11-2018

Field Oriented Sliding Mode Control of Surface-Mounted Permanent Magnet AC Motors: Theory and Applications to Electrified Vehicles

Xin Wang

Max Reitz

Edwin E. Yaz

IEEE Transactions on Vehicular Technology, Vol. 67, No. 11 (November 2018): 10343-10356. DOI.

Field Oriented Sliding Mode Control of Surface-Mounted Permanent Magnet AC Motors: Theory and Applications to Electrified Vehicles

Xin Wang
Department of Electrical and Computer Engineering, Southern Illinois University, Edwardsville, IL,
Max Reitz
Department of Electrical and Computer Engineering, Southern Illinois University, Edwardsville, IL
Edwin E. Yaz
Department of Electrical and Computer Engineering, Marquette University, Milwaukee, WI,

Abstract:

Permanent magnet ac motors have been extensively utilized for adjustable-speed traction motor drives, due to their inherent advantages including higher power density, superior efficiency and reliability, more precise and rapid torque control, larger power factor, longer bearing, and insulation life-time. Without any proportional-and-integral (PI) controllers, this paper introduces novel first- and higher-order field-oriented sliding mode control schemes. Compared with the traditional PI-based vector control techniques, it is shown that the proposed field oriented sliding mode control methods improve the dynamic torque and speed response, and enhance the robustness to parameter variations, modeling uncertainties, and external load perturbations. While both first- and higher-order controllers display excellent performance, computer simulations show that the higher-order field-oriented sliding mode scheme offers better performance by reducing the chattering phenomenon, which is presented in the first-order scheme. The higher-order field-oriented sliding mode controller, based on the hierarchical use of supertwisting algorithm, is then implemented with a Texas Instruments TMS320F28335 DSP hardware platform to prototype the surface-mounted permanent magnet ac motor drive. Last, computer simulation studies demonstrate that the proposed field-oriented sliding mode control approach is able to effectively meet the speed and torque requirements of a heavy-duty electrified vehicle during the EPA urban driving schedule.

SECTION I. Introduction and Motivation

Thanks to the latest development of AC electric motors and battery technologies, a wide range of electrified vehicles hit the production line and become commercially available. From the rise of electrified heavy-duty trucks, such as Tesla Semi-truck, to the huge market growth of passenger-type hybrid electric vehicles, such as Toyota Prius, the future of transportation industry and market will be dominated by all types of electrified vehicles, including pure electric vehicles (PEVs), hybrid electric vehicles (HEVs), and fuel-cell vehicles (FCVs).

Besides reduction of the carbon dioxide emission and high energy efficiency, the three distinct advantages of electrified vehicles have been summarized by Hori in [1] as follows:

1. *Precise and fast toque generation from electric motors:* The electric motor's torque response is typically within several milliseconds, whereas the response of an internal combustion engine or a hydraulic braking system is 10 to 100 times slower. Utilizing this essential feature, advanced control of traction motors enables dynamically changing the vehicle's characteristics without changing the driver's behavior. Anti-lock braking system (ABS) and traction control system (TCS) can be cooperated and integrated together, since motor can produce both acceleration and deceleration torques. Battery energy savings can be optimized by using regenerative braking and low-drag tires.
2. *A motor can be attached to each wheel:* Toque from smaller-sized motor-wheel sets can be controlled independently and cooperatively, which leads to safety and performance improvements of electrified vehicles. Distributed motor location can enhance the performance of vehicle stability control (VSC), which is not achievable in traditional internal combustion engine (ICE) based vehicles.
3. *Motor torque can be easily measured:* The driving and braking torque generated from electric motors enjoys much smaller uncertainties, compared to that of an IC engine or hydraulic brake. Based upon current measurement, driving force observer can be developed to estimate the driving and braking force between tire and road in real-time, which enables control technologies to safely governs the vehicle traction based on road condition estimation.

For aforementioned electrified vehicles traction control, adjustable speed permanent magnet AC motor (PMAC) drives have been extensive employed. As an example, the 8-pole interior-mounted permanent magnet AC motors (IPMs) are commonly used in Toyota Prius for traction and regenerative braking. The popularity of poly-phase permanent magnet AC motors should be attributed to their inherent advantages of more accurate and faster torque control, larger torque to inertia ratio, higher power density, longer bearing and insulation life-time, larger power factor, superior efficiency and reliability, when compared to other types of electric motor drives.

Over the past decades, the vast majority of academic and industrial effort approaches high performance real-time PMAC motor control challenge by means of *field oriented control* (FOC) and *direct torque control* (DTC) [2], also known as vector control. Without the large current harmonics or torque ripples inherent in direct torque control [3]- [6], field oriented control is traditionally executed through proportional-integral (PI) controllers. Although a PI controller enjoys the advantage of simplicity and the ease of implementation, its design process suffers from the following distinct drawbacks:

1. A PI controller may not provide satisfactory transient performance, since it does not take *load perturbations, external disturbances, parameters variations and modeling uncertainties* into account. Therefore, a PI controller is not a very robust linear controller.
2. In order to design PI-based field oriented controllers, *decoupling system is needed to convert the nonlinear PM motor dynamics into classical single-input-single-output (SISO) systems*, so that PI control gain can be computed based on the chosen phase and gain margins to meet the stability requirements of linear control. Discrepancies between the actual nonlinear PMAC motor dynamics and the linear SISO models employed for PI controller design deteriorate the field oriented control performance, in which the stability of closed-loop feedback AC motor control systems is also compromised.

Actually, in additional to coupled nonlinearities, permanent magnet synchronous motor drives face with parameter variations, modeling uncertainties and extraneous load perturbations. Unfortunately, conventional linear control approaches, including aforementioned proportional-integral (PI) approach and linear quadratic regulator (LQR) method cannot achieve sufficiently high performance for permanent magnet AC motor systems due to the inherent limitations. Hence, a high performance nonlinear control scheme would be desirable to overcome these difficulties in practical electrified vehicle applications, which guarantees fast and stable transient behavior, quick toque and speed recovery from disturbances and perturbations, and robustness against system parameter variations and modeling uncertainties.

To address this application-oriented challenge, many nonlinear control methods have been recently developed as compelling alternatives to classical PI controllers. These nonlinear controls include fuzzy control, robust control, state dependent Riccati equation based control, model predictive control, feed-forward control, adaptive control, intelligent control, neural-network control, feedback linearization, and sliding mode control, which have been studied and reported in literature [7]–[32] . In [7], the fuzzy control methods have limitations to choose the appropriate membership functions and fuzzy rules for the fuzzy inference motion control system. Robust control, such as H_∞ control method in [8], requires complicated design processes and much more complicated numerical solvers to compute the control solution. The state dependent Riccati equation control requires the solutions from Riccati equation at each time-step [9], [10] . If the Riccati equation solution is infeasible, then the motor control is failed. In [11], model predictive control (MPC) can provide good performance in instantaneous current control for motor drive, but MPC is not robust. An intelligent control or a neural network-based control technique requires a huge amount of computation complexity, while its control performance is not guaranteed, and there is no stability warranty [12], [13]. Linear quadratic regulator (LQR) based optimal vector control of PMSM in dq synchronous coordinate frame with state feedback is reported in [14]. However, LQR optimal control is designed for torque and speed regulation around the steady-state operating point. Furthermore, LQR control is not robust, and can be sensitive to model uncertainties, external disturbances and extraneous noise. [15] proposes a modified vector-controlled IPM drive system with the purpose of minimizing copper losses based upon a voltage-constrained tracking in the field weakening control. The approach is designed based on steady state voltage equations, i.e. the time derivatives of currents are ignored. [16] presents a combined adaptive control, fuzzy logic, neural network and genetic algorithm based control of a linear induction motor drive, which is complicated to be implemented in practice, and without stability guarantee. Different from the feedback linearization method used in [17], [18] applies the Hamiltonian of nonlinear optimal control theory to achieve the feedback linearization control of PM synchronous machines operating with varying speed/torque. Feedback linearziation requires transformation must be a diffeomorphism, i.e., the transformation must be invertible. But in practice, the transformation of motor model can only be locally diffeomorphic, the feedback linearziation results only hold within a small neighborhood of equilibrium point, therefore, the method in [18] also have limitations for practical motor-drive applications.

It should be mentioned the Maximum Torque Per Ampere (MTPA) control technique has been widely utilized as a practical interior-mounted permanent magnet synchronous motor (IPM) motion control solution [19]–[23]. For a given magnitude of current vector, the stator current vector can be controlled using MTPA control to maximize the developed torque. The MTPA method has been extensively used, as it can be conveniently implemented with PI controllers, while minimizing the copper loss. However, MTPA cannot be applied above the rated speed due to the voltage limit. [19] proposes the high-performance current regulator to improve current responses in high-speed flux-weakening region by a feed-forward compensator. This control strategy has been widely adopted in constant torque operating range to achieve fast transient and high-efficiency operation of IPM drive systems.

Sliding modes are well-known for their robustness against parameter variations, modeling uncertainties, external disturbances and perturbations in the mathematical description of physical systems [24]-[32]. Compared with a proportional-integral (PI) controller, a sliding mode scheme improves the dynamic performance, reduces the response-time and overshoot, provides perfect decoupling, and enhances the overall stability of permanent magnet AC motor drives.

Extending our previous effort in [33], [34], where we focus on first and higher-order sliding mode theory development, this manuscript presents novel first and higher-order *field oriented sliding mode control* strategies to develop high performance surface-mounted permanent magnet AC motor drives (SPMs) operating smoothly and robustly over the full-speed range, with the maximized electromechanical torque output. The main contributions of this manuscript are summarized as follows:

1. The proposed *field oriented sliding mode control* scheme (FOSMC) enjoys the combined advantages of field oriented control and sliding mode control. On the one hand, the field oriented control scheme maximizes the developed electromechanical torque by setting the flux and stator current vectors orthogonal with each other, since the developed electromechanical torque can be expressed as the outer product of the two vectors. On the other hand, the sliding mode control scheme can guarantee faster transient behavior, less overshoot, smaller steady state error, less sensitive to model parameter variations and load torque perturbations, when compared to PI or LQR based linear controllers.

2. This manuscript approaches the chattering problem by utilizing the novel higher-order FOSMC control method based on the hierarchical use of the super-twisting algorithm. The ideal property of super-twisting algorithm (STA) is that it does not require any time-derivatives of the sliding variables.
3. To confirm the effectiveness and robustness of the proposed field oriented sliding mode control, experiments are carried out with computer simulations and hardware implementations involving a Texas Instruments TMS320F28335 DSP based prototype platform.
4. A heavy-duty hybrid electric vehicle is modeled and controlled with the proposed higher-order sliding mode controller. The EPA Urban Dynamometer Driving Schedule (UDDS) is used for the reference test-drive input to the vehicle. Simulation studies verify that the proposed controller is able to nearly perfectly track the speed reference.

The remainder of this manuscript is structured as follows: Section II establishes the dynamic modeling of surface-mounted permanent magnet synchronous motors. The proposed field oriented sliding mode control scheme is introduced and compared with the traditional proportional-integral (PI) based field oriented control scheme. Section III presents the overview of sliding mode control theory. Section IV gives the detailed derivation of the first-order field oriented sliding mode controller. Section V presents the detailed design of the higher-order sliding mode controller. The implementation of Texas Instruments TMS320F28335 DSP based platform are summarized in Section VI. Section VII provides the modeling of hybrid electric vehicle, and numerical simulation of hybrid electric vehicle controlled with the field-oriented sliding mode control under the UDDS driving cycle. Finally, we conclude the paper in Section VIII by highlighting directions for future work.

SECTION II. Dynamics of Surface-Mounted Permanent Magnet AC Motors

Consider the dq synchronous frame model of a 3-phase surface-mounted permanent magnet synchronous motor (SPM) given as [35] :

$$\frac{di_d}{dt} = -\frac{R_s}{L} i_d + \frac{P}{2}\omega_r i_q + \frac{1}{L}u_d \quad (1)$$

$$\begin{aligned}\frac{di_q}{dt} &= -\frac{R_s}{L} i_q - \frac{P}{2}\omega_r i_d - \frac{P}{2}\omega_r \frac{\Phi_m}{L} + \frac{1}{L}u_q \\ \frac{d\omega_r}{dt} &= \frac{\tau_e}{J} - \frac{\tau_m}{J} - \frac{B\omega_r}{J},\end{aligned} \quad (2)(3)$$

where u_d and u_q are the stator voltage component defined in dq synchronous reference frame; i_d and i_q are the stator current components defined in dq synchronous reference frame; ω_r is the rotor speed in mechanical rad/sec.; P is the number of poles; Φ_m is the permanent magnet rotor flux linkage; J is the rotor moment of inertia; B is the viscous damping coefficient; τ_m is the load torque; R_s is the armature winding resistance; and L is the stator inductance. The developed electromechanical torque τe can be expressed as:

$$\tau_e = \frac{3P}{4}\Phi_m i_q \quad (4)$$

It should be noted that for SPM, there is no reluctance torque component existed in (4), since the direct- and quadrature-axis stator inductances are the same, i.e., $L_d = L_q = L$.

Notice that motor dynamics (1)– (3) are cross-coupled nonlinear equations. For traditional field oriented control scheme, the development of proportional-integral (PI) based controllers requires decoupling and back-emf compensation as shown in (6). Decoupling systems are essential to convert the nonlinear coupled dynamics into single-input-single-output linear models. By performing the decoupling stage as shown in Fig. 1, the two inputs to space-vector pulse-width-modulation scheme, u_d and u_q, can be expressed as

$$\begin{aligned} u_d &= (PI)(i_d^* - i_d) - \tfrac{P}{2}\omega_r L i_q \\ u_q &= (PI)(i_q^* - i_q) + \tfrac{P}{2}\omega_r L i_d + \tfrac{P}{2}\omega_r \Phi_m \end{aligned} \quad (5)(6)$$

where PI stands for a standard proportional-integral controller.

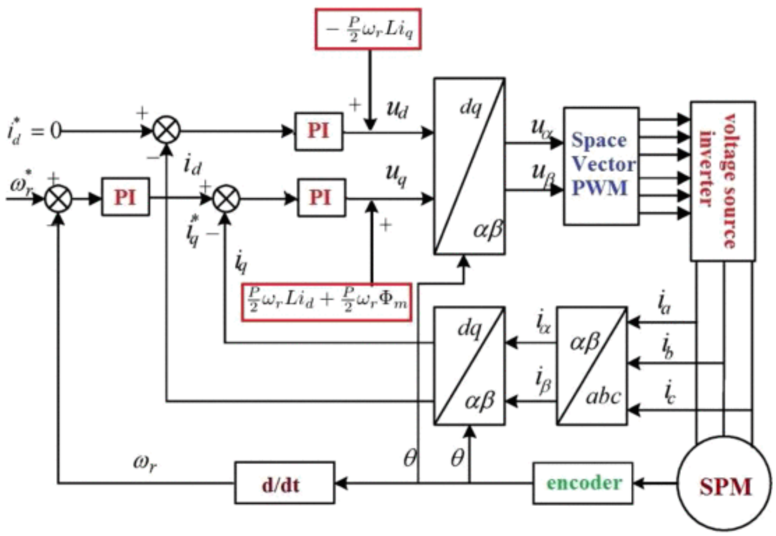

Fig. 1. Block diagram of the traditional proportional-integral based field oriented control.

Different from the traditional PI-based field oriented scheme, the proposed field-oriented sliding mode control of surface-mounted permanent magnet AC motors (SPMs) does not involve any decoupling blocks as shown in Fig. 2. With the measurement feedback of i_d, i_q , ω_r, the proposed field oriented sliding mode control can be achieved by implementing velocity sliding mode controller, flux sliding mode controller and torque sliding mode controller. The orthogonality of flux and current space vectors are guaranteed by aligning the armature current vector along the q-axis, i.e., $i_d^* = 0$, and the flux vector along the d-axis. An encoder or resolver-to-digital converter (RDC) can provide the mechanical rotor position θ_r and speed ω_r information in real-time as shown in Fig. 2.

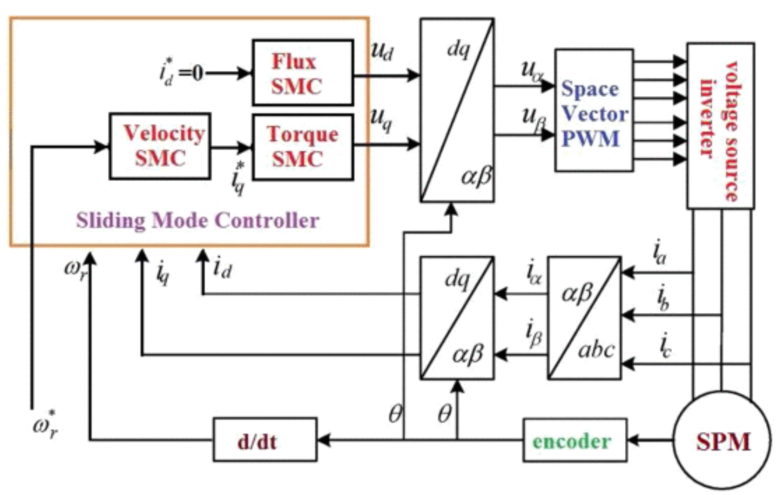

Fig. 2. Block diagram of the proposed field oriented sliding mode control.

SECTION III. Sliding Mode Control Theory

One of the most intriguing aspects of a sliding mode controller is that by utilizing a discontinuous control approach whose primary function is to rapidly switches between two distinct continuous manifolds, the controlled system dynamics is forced to track a predetermined trajectory known as the sliding surface [30], [31].

Consider the following input-affine nonlinear dynamics

$$\dot{x}(t) = f(x,t) + h(x,t) \cdot u(t), \quad (7)$$

where $x \in \mathcal{R}^n$ denotes the state-space variable. $f(x,t)$ and $h(x,t)$ are smooth $n \times n$ and $n \times m$ nonlinear vector functions, respectively. The discontinuous control input $u \in \mathcal{R}^m$ is expressed as

$$u = \begin{cases} U^+(x,t) & \text{if } s(x) > 0 \\ U^-(x,t) & \text{if } s(x) < 0 \end{cases}, \quad (8)$$

where $s(x) = (s_1(x), \ldots, s_m(x))^T$ defines the sliding manifold, while $s_i(x) = 0, \forall i = 1 \ldots m$ describe the m sliding surfaces.

The aforementioned closed-loop control system exhibits sliding mode properties if the following reachability, existence, and stability conditions are satisfied:

1) *Reachability condition:* ensures that state trajectory will approach and eventually reach the sliding manifold, by satisfying the following condition:

$$s(x,t)\dot{s}(x,t) < 0 \quad (9)$$

2) *Existence condition:* guarantees that once state trajectory is within the neighborhood of sliding manifold, it will be directed toward the sliding surface, by meeting the following requirement:

$$\lim_{s \to 0} s(x,t)\dot{s}(x,t) < 0 \quad (10)$$

3) *Stability condition:* secures that the sliding manifold will direct the state trajectory toward the stable equilibrium point, which can be obtained by checking the stability in steady-state.

Now, we are in the position to describe the main results, which provide optimal and robust solutions for the field oriented sliding mode control of a surface-mounted permanent-magnet synchronous motor.

A. Sliding Surfaces

The sliding manifold $s(x,t) = (s_d, s_q, s_{\omega_r})^T$ of the field-oriented sliding mode control is governed by

$$\begin{aligned} s_d &= i_d - i_d^* = 0 \\ s_q &= i_q - i_q^* = 0 \\ s_{\omega_r} &= \omega_r - \omega_r^* = 0 \end{aligned} \quad (11)(12)(13)$$

B. Parameter Uncertainties

Considering modeling uncertainties, unmodeled dynamics, and parameter variations in the permanent magnet AC motor dynamics, the following notations are introduced: $R_s = \hat{R}_s + \Delta R_s$; $L = \hat{L} + \Delta L$; $\Phi_m = \hat{\Phi}_m + \Delta\Phi_m$; $\tau_m = \hat{\tau}_m + \Delta\tau_m$; $J = \hat{J} + \Delta J$; and $B = \hat{B} + \Delta B$. Note that $\hat{\cdot}$ denotes the nominal value, and $\Delta \cdot$ denotes the bounded parameter uncertainty/variation.

SECTION IV. First-Order Sliding Mode Control Design

A. First-Order Flux Sliding Mode Control

The d-axis magnetic-flux control law is given as

$$u_d = u_{d,eq} + u_{d,N} \quad (14)$$

where u_d is the direct-axis stator voltage, $u_{d,eq}$ is the equivalent control and $u_{d,N}$ is the switching control.

The equivalent control can be obtained from $\dot{s}_d = 0$.

$$\dot{s}_d = \frac{1}{L}\left[-R_s i_d + \frac{P}{2}\omega_r L i_q + u_d - L\frac{di_d^*}{dt}\right] \quad (15)$$

Solving for $u_{d,eq}$ results in

$$u_{d,eq} = \hat{R}_s i_d - \frac{P}{2} w_r \hat{L} i_q + \hat{L}\frac{di_d^*}{dt} \quad (16)$$

Equivalently, $\dot{s}_d$ in (15) can be represented as

$$\dot{s}_d = \frac{1}{L}\left[-\Delta R i_d + \frac{P}{2}\omega_r \Delta L i_q + u_{d,N} - \Delta L\frac{di_d^*}{dt}\right] \quad (17)$$

Based upon LaSalle's invariance principle, we can obtain the switching control component guaranteeing the Lyapunov stability. Since the uncertainties present in the parameters are bounded, there exists a positive upper-bound u_{d0}, such that

$$u_{d0} > \left|\Delta R i_d + \Delta L\frac{di_d^*}{dt} - \frac{P}{2}\omega_r \Delta L i_q\right| \quad (18)$$

The switching control component of u_d is then obtained as

$$u_{d,N} = -u_{d0}\, sgn(s_d), \quad (19)$$

where the signum function $sgn()$ is known as

$$sgn(s) = \begin{cases} 1 & \text{if } s > 0 \\ 0 & \text{if } s = 0 \\ -1 & \text{if } s < 0 \end{cases} \quad (20)$$

B. First-Order Torque Sliding Mode Control

The q-axis torque control law is given as:

$u_q = u_{q,eq} + u_{q,N}$, (21)

where u_q is the quadrature-axis stator voltage, $u_{q,eq}$ is the equivalent control and $u_{q,N}$ is the switching control.

Using the aforementioned method, we first derive $\dot{s}_q$ to be

$$\dot{s}_q = \frac{1}{L}\left[-R_s i_q - \frac{P}{2}\omega_r \Phi_m - \frac{P}{2}\omega_r L i_d + u_q - L\frac{di_q^*}{dt}\right] \text{ (22)}$$

The q-axis equivalent control can be obtained as follows

$$u_{q,eq} = \hat{R}_s i_q + \frac{P}{2}\omega_r \hat{L} i_d + \frac{P}{2}\omega_r \hat{\Phi}_m + \hat{L}\frac{di_q^*}{dt} \text{ (23)}$$

$\dot{s}_q$ is then rewritten as

$$\dot{s}_q = \frac{1}{L}\left[-\Delta R i_q - \frac{P}{2}\omega_r \Delta\Phi_m - \frac{P}{2}\omega_r \Delta L i_d + u_{q,N} - \Delta L\frac{di_q^*}{dt}\right] \text{ (24)}$$

Similarly, since the parameter uncertainties are all bounded, there exists a positive upper-bound u_{q0}, such that

$$u_{q0} > \left[\Delta R i_q + \frac{P}{2}\omega_r \Delta L i_d + \frac{P}{2}\omega_r \Delta\Phi_m + \Delta L\frac{di_q^*}{dt}\right] \text{ (25)}$$

The switching control component of u_q is then obtained as

$$u_{q,N} = -u_{q0} sgn(s_q) \text{ (26)}$$

The q-axis torque control action keeps i_q converging to the desired reference q-axis stator current i_q^*.

C. First-Order Velocity Sliding Mode Control

We define the q-axis velocity control law as

$i_q^* = i_{q,eq}^* + i_{q,N}^*$, (27)

where i_q is the quadrature-axis stator current, $i_{q,eq}$ is the equivalent control and $i_{q,N}$ is the switching control.

From the sliding surface s_{ω_r}, $\dot{s}_{\omega_r}$ is found to be

$$\dot{s}_{\omega_r} = \frac{3P\Phi_m}{4J} i_q - \frac{\tau_m}{J} - \frac{B\omega_r}{J} - \frac{d\omega_r^*}{dt} \text{ (28)}$$

The equivalent control becomes:

$$i_{q,eq}^* = \frac{1}{K_t}\left[\hat{\tau}_m + \hat{B}\omega_r + \hat{J}\frac{d\omega_r^*}{dt}\right], \text{ (29)}$$

where

$K_t = \frac{3}{4} P \Phi_m$. (30)

Following the similar procedure as the previous control designs, there exists a positive upper-bound i_{q0}, such that

$$i_{q0} > \left[\frac{1}{K_t}\left(\Delta\tau_m + \Delta B\omega_r + \Delta J\frac{d\omega_r^*}{dt}\right)\right] \quad (31)$$

The switching control component of i_q^* is then obtained as

$$i_{q,N}^* = -i_{q0}sgn(s_{\omega_r}) \quad (32)$$

The output of q-axis velocity control, i_q^*, serves as the input to q-axis torque sliding mode control in Section IV Part B.

SECTION V. Higher-Order Sliding Mode Control Design

The oscillatory dynamic behavior about the sliding manifold, commonly known as chattering, exists in the first-order sliding mode scheme. Chattering effect, which is caused by the imperfections of switching devices, is the major drawback of the first-order approach. To eliminate the chattering phenomenon, the second-order sliding mode control methods is developed using the super-twisting algorithm (STA). Some preliminary results on higher-order sliding mode control are given in [30]. Sliding manifolds s for higher-order sliding modes are chosen to be the same as the first-order sliding manifolds. Therefore, the equivalent controls for higher-order sliding modes are the same ones for first-order sliding modes. STA can be summarized as follows:

Let $y_1 = s, y_2 = \dot{s}$, then

$$\begin{aligned} \dot{y}_1 &= y_2 = \dot{s} = \frac{\partial s}{\partial t} + \frac{\partial s}{\partial x}\dot{x} \\ \dot{y}_2 &= \ddot{s} = (\frac{\partial \dot{s}}{\partial t} + \frac{\partial \dot{s}}{\partial x}\dot{x}) + \frac{\partial \dot{s}}{\partial u}\dot{u} = \psi(x,t) + \gamma(x,t)\dot{u} \end{aligned} \quad (33)$$

where

$$\begin{aligned} |\psi| &\leq \Psi > 0 \\ 0 &< \Gamma_m \leq \gamma \leq \Gamma_M, \end{aligned} \quad (34)$$

with the lower-bound and the upper-bound of γ denoted as Γ_m and Γ_M, respectively.

The switching control algorithm is defined by the following control law:

$$\tilde{u} = u_1 + u_2 \quad (35)$$

with

$$\begin{aligned} \dot{u}_1 &= -Wsgn(y_1) \\ u_2 &= \begin{cases} -\lambda|s_0|^p sgn(y_1) & |y_1| > |s_0| \\ -\lambda|y_1|^p sgn(y_1) & |y_1| \leq |s_0| \end{cases}, \end{aligned} \quad (36)(37)$$

where W, λ, p are positive sliding mode constants. The corresponding sufficient conditions for finite-time convergence to the sliding surface are given as follows:

$$
\begin{aligned}
W &> \frac{\Psi}{\Gamma_m} \\
\lambda^2 &\geq \frac{4\Psi}{\Gamma_m^2}\frac{\Gamma_M(W+\Psi)}{\Gamma_m(W-\Psi)} \\
0 &< p \leq 0.5
\end{aligned}
\quad (38)(39)(40)
$$

The distinct advantage of super-twisting algorithm (STA) is that it does not require any information of the time derivative of the sliding variables. It is noteworthy that this merit is essential for real-time hardware implementation of the proposed higher-order field oriented sliding mode control (FOSMC).

Also note that, by selecting $p = 1$, the aforementioned control algorithm converges to the sliding surface exponentially, which leads to an exponentially stable 2-sliding mode in the sense of Lyapunov. The selection of $p = 0.5$ ensures that the maximal possible for 2-sliding realization real-sliding order 2 is achieved.

A. Higher-Order Flux Sliding Mode Control

For second-order sliding mode control, both $s(x)$ and $\dot{s}(x)$ are set to be zero. From the Section IV part A results on $\dot{s}_d$

$$\dot{s}_d = \frac{1}{L}\left[-R_s i_d + \frac{P}{2}\omega_r L i_q + u_d - L\frac{di_d^*}{dt}\right] \quad (41)$$

$\ddot{s}_d$ is obtained by taking derivative of (41) as

$$\ddot{s}_d = -\frac{R_s}{L}\frac{di_d}{dt} + \frac{P}{2}\frac{d\omega_r}{dt}i_q + \frac{P}{2}\frac{di_q}{dt}\omega_r + \frac{1}{L}\frac{du_d}{dt} - \frac{d^2 i_d^*}{dt} \quad (42)$$

Denote

$$\psi_d = -\frac{R_s}{L}\frac{di_d}{dt} + \frac{P}{2}\frac{d\omega_r}{dt}i_q + \frac{P}{2}\frac{di_q}{dt}\omega_r - \frac{d^2 i_d^*}{dt} \in [-\Psi_d, \Psi_d] \quad (43)$$

and

$$\gamma_d = \frac{1}{L} \in [\Gamma_{md}, \Gamma_{Md}] \quad (44)$$

Denoting $\zeta_L = |\Delta L| \ll \hat{L}$, we may choose the lower- and upper-bound Γ_{md}, Γ_{Md} as follows

$$
\begin{aligned}
\Gamma_{md} &= \frac{1}{\hat{L}+\zeta_L} > 0, \\
\Gamma_{Md} &= \frac{1}{\hat{L}-\zeta_L} > 0
\end{aligned}
\quad (45)(46)
$$

Control input u_d consists of the sum of equivalent control $u_{d,eq}$ and switching control $\tilde{u}_d$. Note that the equivalent control $u_{d,eq}$ is the same as (16), and the switching control $\tilde{u}_d$ is given as:

$$\tilde{u}_d = u_{d1} + u_{d2} \quad (47)$$

with

$$\dot{u}_{d1} = -W_d sgn(s_d)$$
$$u_{d2} = \begin{cases} -\lambda_d |s_0|^p sgn(s_d) & |s_d| > |s_0| \\ -\lambda_d |s_d|^p sgn(s_d) & |s_d| \leq |s_0| \end{cases} \quad (48)(49)$$

The sufficient conditions for finite-time convergence to the sliding surface are summarized as follows:

$$W_d > \frac{\Psi_d}{\Gamma_{md}}$$
$$\lambda_d^2 \geq \frac{4\Psi_d}{\Gamma_{md}^2} \frac{\Gamma_{Md}(W_d+\Psi_d)}{\Gamma_{md}(W_d-\Psi_d)} \quad (50)(51)(52)$$
$$0 < p \leq 0.5$$

We choose $p = 0.5$ in this manuscript for implementing the proposed higher-order sliding mode control. The controller can be simplified by selecting $s_0 = \infty$. Therefore, we have

$$\tilde{u}_d = -\lambda_d |s_d|^{1/2} sgn(s_d) - W_d \int sgn(s_d) dt \quad (53)$$

B. Higher-Order Torque Sliding Mode Control

The similar method used for the d-axis flux control is applied for developing the q-axis torque sliding mode control. Based on previous analysis in Section IV Part B, $\dot{s}_q$ is expressed as

$$\dot{s}_q = \frac{1}{L}\left[-R_s i_q - \frac{P}{2}\omega_r \Phi_m - \frac{P}{2}\omega_r L i_d + u_q - L\frac{di_q^*}{dt}\right] \quad (54)$$

By taking the second-order derivative, $\ddot{s}_q$ can be obtained as

$$\ddot{s}_q = -\frac{R_s}{L}\frac{di_q}{dt} - \frac{P}{2}\omega_r \frac{di_d}{dt} - \frac{P}{2} i_d \frac{d\omega_r}{dt} - \frac{P}{2}\frac{\Phi_m}{L}\frac{d\omega_r}{dt} + \frac{1}{L}\frac{du_q}{dt} - \frac{d^2 i_q^*}{dt^2} \quad (55)$$

Denote

$$\psi_q = -\frac{R_s}{L}\frac{di_q}{dt} - \frac{P}{2}\omega_r \frac{di_d}{dt} - \frac{P}{2} i_d \frac{d\omega_r}{dt} - \frac{P}{2}\frac{\Phi_m}{L}\frac{d\omega_r}{dt} - \frac{d^2 i_q^*}{dt^2} \in [-\Psi_q, \Psi_q] \quad (56)$$

and

$$\gamma_q = \frac{1}{L} \in [\Gamma_{mq}, \Gamma_{Mq}] \quad (57)$$

Similarly, denoting $\zeta_L = |\Delta L| \ll \hat{L}$, we may choose the lower- and upper-bound Γ_{mq}, Γ_{Mq} as follows

$$\Gamma_{mq} = \frac{1}{\hat{L}+\zeta_L} > 0,$$
$$\Gamma_{Mq} = \frac{1}{\hat{L}-\zeta_L} > 0 \quad (58)(59)$$

Control input u_q consists of the sum of equivalent control $u_{q,eq}$ and switching control $\tilde{u}_q$.

$$u_q = u_{q,eq} + \tilde{u}_q \quad (60)$$

Note that the equivalent control $u_{q,eq}$ is the same as (23), and the switching control $\tilde{u}_q$ is given as

$$\tilde{u}_q = u_{q1} + u_{q2} \quad (61)$$

with

$$\dot{u}_{q1} = -W_q sgn(s_q) \quad (62)$$

$$u_{q2} = \begin{cases} -\lambda_q |s_0|^p sgn(s_q) & |s_q| > |s_0| \\ -\lambda_q |s_q|^p sgn(s_q) & |s_q| \leq |s_0| \end{cases} \quad (63)$$

The sufficient conditions for finite-time convergence to the sliding surface are summarized as follows

$$\begin{aligned} W_q &> \frac{\Psi_q}{\Gamma_{mq}} \\ \lambda_q^2 &\geq \frac{4\Psi_q}{\Gamma_{mq}^2} \frac{\Gamma_{Mq}(W_q+\Psi_q)}{\Gamma_{mq}(W_q-\Psi_q)} \\ 0 &< p \leq 0.5 \end{aligned} \quad (64)(65)(66)$$

The controller can be simplified by selecting $s_0 = \infty$. Hence, $\tilde{u}_q$ can be expressed as

$$\tilde{u}_q = -\lambda_q |s_q|^{1/2} sgn(s_q) - W_q \int sgn(s_q) dt \quad (67)$$

C. Higher-Order Velocity Sliding Mode Control

By applying similar methods, from the Section IV Part C, we have

$$\dot{s}_{\omega_r} = \frac{3P\Phi_m}{4J} i_q - \frac{\tau_m}{J} - \frac{B\omega_r}{J} - \frac{d\omega_r^*}{dt} \quad (68)$$

Therefore, $\ddot{s}_{\omega_r}$ is obtained by taking the second-order derivative of s_{ω_r} as

$$\ddot{s}_{\omega_r} = \frac{K_t}{J}\frac{di_q}{dt} - \frac{1}{J}\frac{d\tau_m}{dt} - \frac{B}{J}\frac{d\omega_r}{dt} - \frac{d^2\omega_r^*}{dt^2} \quad (69)$$

Again, denote

$$\psi_{\omega_r} = -\frac{1}{J}\frac{d\tau_m}{dt} - \frac{B}{J}\frac{d\omega_r}{dt} - \frac{d^2\omega_r^*}{dt^2} \in [-\Psi_\omega, \Psi_\omega] \quad (70)$$

and

$$\gamma_{\omega_r} = \frac{K_t}{J} \in [\Gamma_{m\omega}, \Gamma_{M\omega}] \quad (71)$$

Denoting $\zeta_{\omega} = |\frac{K_t}{J} - \frac{\hat{K}_t}{\hat{J}}| = |\frac{1}{J}(\frac{3}{4}P\Phi_m) - \frac{1}{\hat{J}}(\frac{3}{4}P\hat{\Phi}_m)|$ satisfying the condition $\zeta_{\omega} \ll \frac{\hat{K}_t}{\hat{J}}$, we may choose the lower- and upper-bound $\Gamma_{m\omega}, \Gamma_{M\omega}$ as follows

$$\begin{aligned} \Gamma_{m\omega} &= \frac{\hat{K}_t}{\hat{J}} - \zeta_{\omega} > 0, \\ \Gamma_{M\omega} &= \frac{\hat{K}_t}{\hat{J}} + \zeta_{\omega} > 0 \end{aligned} \quad (72)(73)$$

The velocity control input is given as

$$i_q^* = i_{q,eq}^* + \tilde{i}_q^* \quad (74)$$

and

$$\tilde{i}_q^* = i_{q1} + i_{q2}, \quad (75)$$

where

$$\begin{aligned} \dot{i}_{q1} &= -W_{\omega_r} sgn(s_{\omega_r}) \\ i_{q2} &= \begin{cases} -\lambda_{\omega_r}|s_0|^p sgn(s_{\omega_r}) & |s_{\omega_r}| > |s_0| \\ -\lambda_{\omega_r}|s_{\omega_r}|^p sgn(s_{\omega_r}) & |s_{\omega_r}| \le |s_0| \end{cases} \end{aligned} \quad (76)(77)$$

The sufficient conditions for finite-time convergence to the sliding surface are summarized as follows

$$\begin{aligned} W_{\omega_r} &> \frac{\Psi_{\omega_r}}{\Gamma_{m\omega}} \\ \lambda_{\omega_r}^2 &\ge \frac{4\Psi_{\omega_r}}{\Gamma_{m\omega}^2} \frac{\Gamma_{M\omega}(W_{\omega_r}+\Psi_{\omega_r})}{\Gamma_{m\omega}(W_{\omega_r}-\Psi_{\omega_r})} \\ 0 &< p \le 0.5 \end{aligned} \quad (78)(79)(80)$$

The controller can be simplified by selecting $s_0 = \infty$. Hence, $\tilde{i}_q^*$ is obtained as

$$\tilde{i}_q^* = -\lambda_{\omega_r}|s_{\omega_r}|^{1/2} sgn(s_{\omega_r}) - W_{\omega_r}\int sgn(s_{\omega_r})dt \quad (81)$$

SECTION VI. Experimental Results

A. Computer Simulation Results

The proposed field oriented sliding mode control algorithms have been examined with computer simulation studies. The testing SPM parameters are specified in Table I. The wheel-connected SPM serves as the traction motor of a heavy-duty vehicle, and we can control the torque of each wheel independently. For PI-based traditional field oriented control, the design parameters for all PI-controllers are $K_i = 5, K_p = 50$, which are fine-tuned to reduce the response overshoot and oscillation.

TABLE I Wheel-Connected SPM Specifications

Motor power	80kW
Armature winding resistance	$R_s = 6.5m\Omega$
d- and q-acis stator inductance	$L = 0.538mH$
Permanent magnet rotor flux linkage	$\Phi m = 0.162Wb$
Number of stator poles	$P = 6$
Viscous friction coefficient	$B = 0.0001N.m.sec/rad$
Wheel inertia	$J = 8.2kg \cdot m^2$

Motor power	$80kW$
Armature winding resistance	$R_s = 6.5m\Omega$
d- and q-axis stator inductance	$L = 0.538mH$
Permanent magnet rotor flux linkage	$\Phi_m = 0.162Wb$
Number of stator poles	$P = 6$
Viscous friction coefficient	$B = 0.0001N.m.sec/rad$
Wheel inertia	$J = 8.2kg \cdot m^2$

Fig. 3 shows the rotor speed response. The load toque is changed from 0 Nm to 25 Nm at the time instant of 3 sec. The reference speed is increased from 500 rpm to 1000 rpm at the time instant of 5 sec. The higher-order sliding mode controller shows shorter rise-time, and less chattering compared with the first-order scheme. And the traditional PI-based field oriented control shows the slowest response time, highest sensitivity to external load change, and unsatisfactory speed regulation performance with significant overshoots and undershoots.

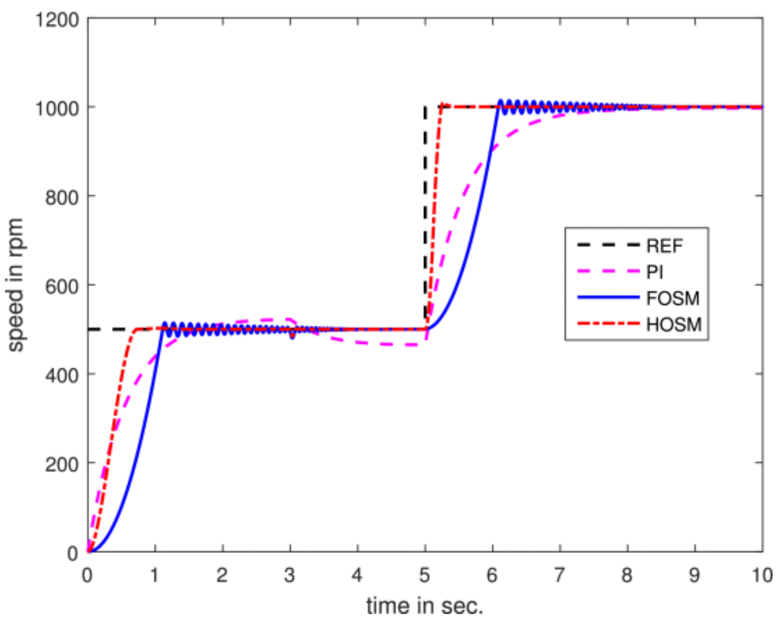

Fig. 3. Speed response to reference speed and load torque changes.

Fig. 4 shows the zoomed-in view of Fig. 3 speed response from 2.95 sec. to 3.15 sec. The sudden load change at 3 sec. in shown in greater detail. The higher-order sliding mode controller provides a faster response to the external load toque change from 0 to 25 Nm. The response of first-order controller can be improved by increasing the gains of switching control at the cost of much excessive chattering phenomenon. PI-based field oriented control shows the slowest response to the external load change with inadequate speed regulations.

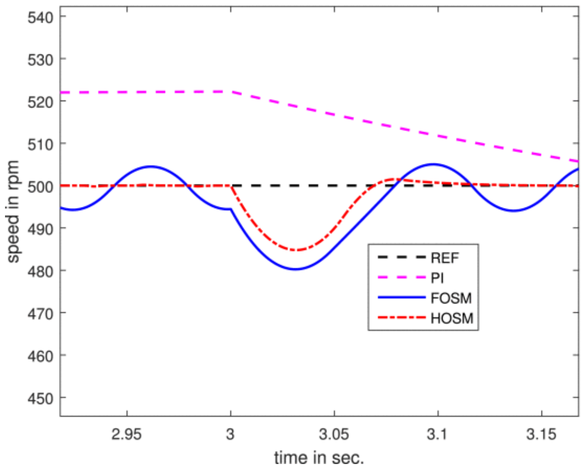

Fig. 4. Speed response to load toque change at 3 sec.

Stator current i_q during the load toque and reference speed change is shown in Fig. 5. The switching control in the first-order scheme causes a high amplitude oscillation in the q -axis current in order to track the reference, and reject external disturbances and parameter uncertainties. The pronounced chattering is effectively reduced in the higher-order sliding mode controller. We did not include the traditional PI-based field oriented control i_q response curve in Fig. 5, since the i_q current with PI-control is significantly higher as shown in Fig. 6. Greater stator current i_q means that the traditional PI-based field oriented control (PI-FOC) based motor drive consumes significantly more electrical power from the battery pack.

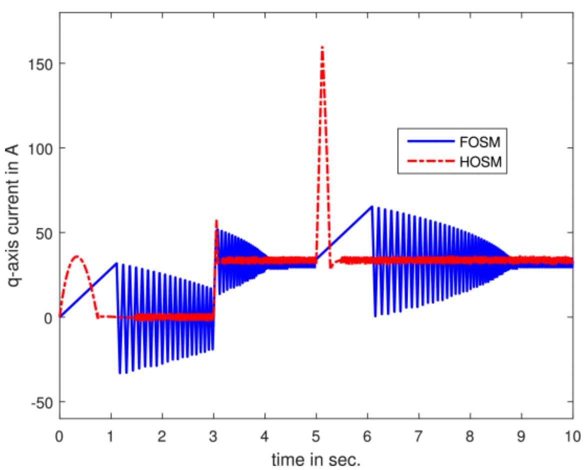

Fig. 5. iq response to reference speed and load torque changes with the field oriented sliding mode control (FOSMC).

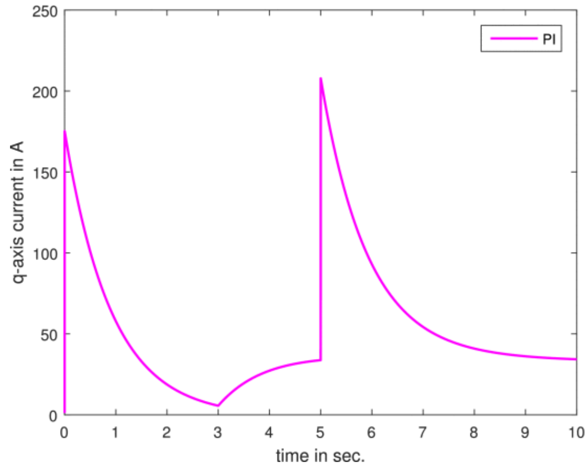

Fig. 6. iq response to reference speed and load torque changes with the traditional PI-based field oriented control (PIFOC).

Stator current i_d is regulated to zero by the first- and higher-order sliding mode scheme, for achieving the field-oriented control performance, as shown in Fig. 7. A closer look of the i_d response is shown in Fig. 8, which shows the significant chattering reduction by using the super-twisting algorithm (STA) based higher-order field oriented sliding mode control.

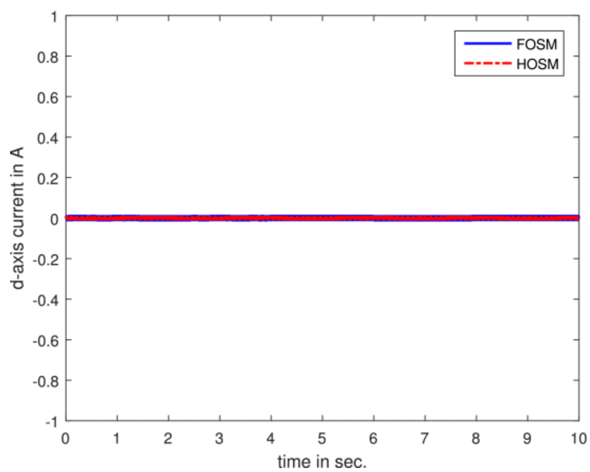

Fig. 7. id response to reference speed and load torque changes with the field oriented sliding mode control (FOSMC).

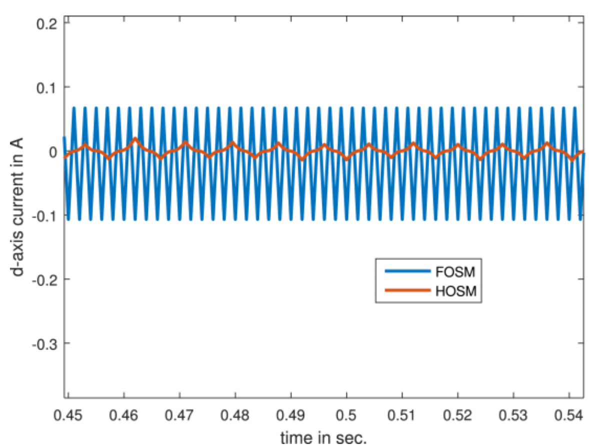

Fig. 8. zoomed-in i_d response with the field oriented sliding mode control (FOSMC).

Again, we did not include the traditional PI-based field oriented control i_d response curve in Fig. 7, since the i_d current with PI-control is significantly larger in magnitude as shown in Fig. 9. Greater stator currenti_d means that the traditional PI-based field oriented controlled motor drives have greater electrical power usage from the battery pack. The proposed field oriented sliding mode control contributes significantly to the energy saving of battery-pack.

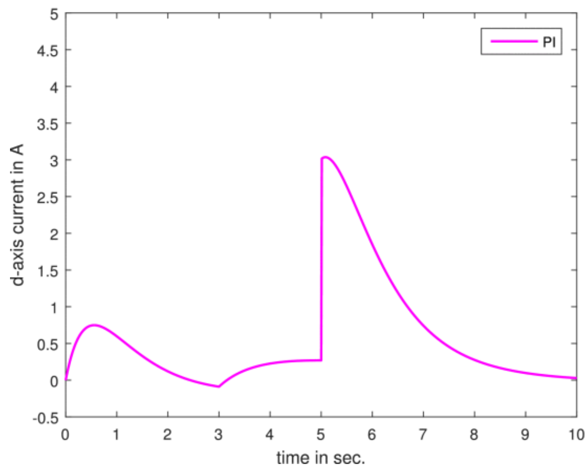

Fig. 9. id response to reference speed and load torque changes with the traditional PI-based field oriented control (PIFOC).

Based on the conducted simulation results, proportional-integral (PI) control is found to provide slower response in speed and torque control with pronounced overshoots and undershoots. PI-control is much more sensitive to external load changes, disturbances and modeling uncertainties. For different load values, the K_p, K_icontrol parameters should be readjusted, if possible, to provide a more decent torque and speed response. PI-control based motor drives consume greater amount of stator currents, which opens the new possibility that the battery usage can be further improved and optimized though advanced vehicle motion control technologies.

While both first- and higher-order field-oriented sliding mode controllers provide excellent dynamic performance in speed and torque response, computer simulation results verify that the higher-order sliding mode control method eliminates chattering in the first-order sliding mode scheme, becomes more robust to external load variations, rejects modeling parameters variation, and offers superior performance of quick and accurate torque generation for SPM motors.

B. Hardware Experimental Results

As shown in Fig. 10, the experiment is performed with a three-phase Anaheim Automation EMJ-04APA22, 0.4kW, 200V, 2.7A, 3000RPM permanent magnet synchronous motor. The SPM is powered by POWEREX PS21765, 600V, 20A, dual-in-line intelligent power module, which includes 6-IGBT inverter, and 3 half-bridge high-voltage integrated-circuit (HVIC) for IGBT gate driving. Space-vector pulse-width-modulation (SVPWM) is used as modulation strategy. The PWM voltage source inverter switching frequency is 10 kHz, while the PWMDAQ is 60kHz. The Texas Instruments 150MHz floating-point TMS320F28335 DSP controller is used, which is a 32 bit floating point digital signal processors with analog interface, RS232 and JTAG emulator port. The TMS320F28335 microprocessor is integrated on the TMDSCNCD28335 controlCARD board, which has analog-to-digital converter (A/D) with 16 channels. The proposed field oriented sliding mode control algorithms have been examined and implemented in real-time with the Texas Instrument TMS320F28335 DSP hardware platform. The parameters and specifications of Anaheim Automation EMJ-04APA22 PMSM are summarized in Table II.

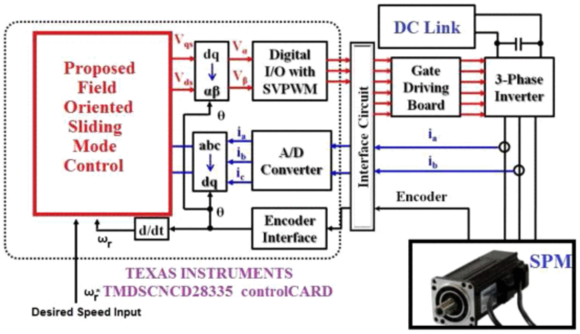

Fig. 10. Experimental setup of prototype SPM drive system with Texas Instruments TMS320F28335 DSP.

TABLE II Anaheim Automation EMJ-04APA22 SPM Parameters

Rated Power	400W
Rated Torque	180 $oz.in$
Rated Voltage	220 $Vrms$
Rated Current	2.7 A
Rated Speed	3000 rpm
Armature winding resistance	$R_s = 4.7\eta\Omega$
d- and q-axis inductance	$L = 13.3mH$
Permanent magnet rotor flux linkage	$\Phi m = 0.0785 Wb$
Number of stator poles	$P = 8$
Viscous friction coefficient	$B = 0.0001 N.m.sec./rad$
Rotor moment of inertia	$J = 0.00439 oz.in.sec^2$
Weight	5.52 lbs

Rated Power	$400W$
Rated Torque	$180oz.in$
Rated Voltage	$220Vrms$
Rated Current	$2.7A$
Rated Speed	$3000rpm$
Armature winding resistance	$R_s = 4.7\Omega$
d- and q-axis inductance	$L = 13.3mH$
Permanent magnet rotor flux linkage	$\Phi_m = 0.0785Wb$
Number of stator poles	$P = 8$
Viscous friction coefficient	$B = 0.0001N.m.sec./rad$
Rotor moment of inertia	$J = 0.00439oz.in.sec^2$
Weight	$5.52lbs$

Fig. 11 shows the experimental result of motor speed response with a reference speed of 2000 rpm. A step input speed reference is applied around 3 sec. Based on the DSP hardware experimental results, it is found that the higher-order field oriented sliding mode control (FOSMC) based SPM motor drive can provide quick and accurate real-time motion control. While PI-based traditional field oriented control shows overshoot and relatively slower response time. And the first-order field oriented sliding mode control shows quite significant chattering.

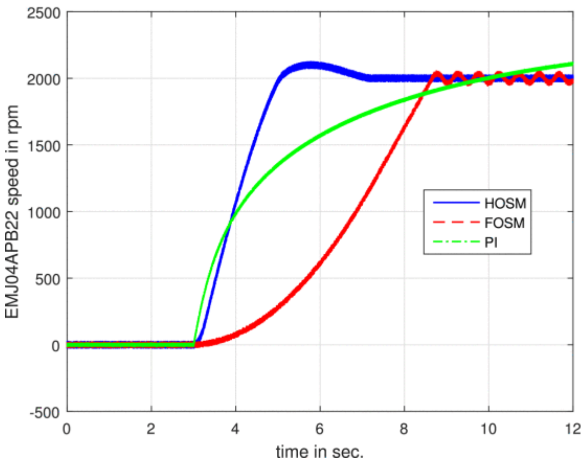

Fig. 11. Anaheim Automation EMJ-04APA22 SPM speed response.

SECTION VII. Applications to Hybrid Electric Vehicles

Electrified vehicles is the most exciting target of advanced motion control technologies. The proposed field oriented sliding mode control (FOSMC) is applied for motion control of a heavy-duty diesel hybrid electric vehicle (HEV) to prove the effectiveness of this new method.

A. Vehicle Specifications

To reduce the energy consumption and improve vehicle's dynamic performance, the drive-train of this vehicle is composed of a V8 turbocharged diesel internal combustion engine (ICE) and 4 surface-mounted permanent magnet synchronous motors (SPMs). Regenerative braking is also considered in the computer simulation. Table III–VI summarize the detailed specifications of this heavy-duty diesel-HEV. And the overall vehicle structure is sketched in Fig. 12.

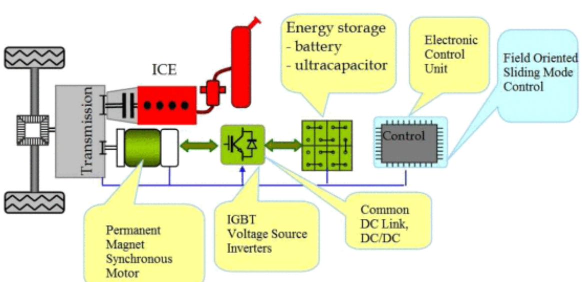

Fig. 12. Hybrid electric vehicle block diagram.

TABLE III Vehicle Specifications

Vehicle Mass	$10340kg$
Radius of Vehicle Wheel	$0.4131m$

Vehicle Mass	$10340kg$
Radius of Vehicle Wheel	$0.4131m$

TABLE IV Transmissions Specifications

Transmission: 1st Gear Ratio	3 .45

Transmission: 2nd Gear Ratio	2.24
Transmission: 3rd Gear Ratio	1.41
Transmission: 4th Gear Ratio	1
Transmiss ion: 1st Gear Efficiency	0.9893
Transmission: 2nd Gear Efficiency	0.966
Transmission: 3rd Gear Efficiency	0.9957
Transmission: 4th Gear Efficiency	1
Prop-shafts/Differential: Differential Drive Ratio	3.21
Prop-shafts/Differential: Differential Efficiency	0.96

Transmission: 1st Gear Ratio	3.45
Transmission: 2nd Gear Ratio	2.24
Transmission: 3rd Gear Ratio	1.41
Transmission: 4th Gear Ratio	1
Transmission: 1st Gear Efficiency	0.9893
Transmission: 2nd Gear Efficiency	0.966
Transmission: 3rd Gear Efficiency	0.9957
Transmission: 4th Gear Efficiency	1
Prop-shafts/Differential: Differential Drive Ratio	3.21
Prop-shafts/Differential: Differential Efficiency	0.96

TABLE V Diesel ICE Specifications

Configuration	VS Turbocharged, Intercooled
Dis place ment	7.3L
Bore	10.44cm
Connecting Rod Length	18.11cm
Compression Ratio	17.4cm
Cutoff	2
Combustion Efficiency	1
Rated Peak Power	210hp@2410r pm ,
Rated Peak Torque	*520lb ft @l 500r pm ,*
Heati ng Value of Diese l QLHV	*43000000 J / kg*
Fuel Density	800

Configuration	V8 Turbocharged, Intercooled
Displacement	$7.3L$
Bore	$10.44cm$
Connecting Rod Length	$18.11cm$
Compression Ratio	$17.4cm$
Cutoff	2
Combustion Efficiency	1
Rated Peak Power	$210hp$@$2410rpm$,
Rated Peak Torque	520*lb-ft*@$1500rpm$,
Heating Value of Diesel QLHV	$43000000J/kg$
Fuel Density	800

TABLE VI Electric Motor Specifications

Electric Drivetrain	Vheel-Connected SPMs in Tab. 1

Electric Drivetrain	Wheel-Connected SPMs in Tab. I

The EPA Urban Dynamometer Driving Schedule (UDDS), which is commonly known as the ”LA4” or ”the city test” and represents city driving conditions [36], is applied as the driving schedule for this diesel-HEV simulation study.

B. Diesel-HEV Modeling and Vehicle Operation Modes

The power required by the diesel hybrid electric vehicle is

$$\dot{W}_{req} = [R_L + (M + M_r)a]v, \text{ (82)}$$

where $\dot{W}_{req}$ is the power required at the wheels to accelerate the vehicle and overcome drag, rolling resistance, and climbing force. The vehicle speed is v and the acceleration is a. The road load is

$$R_L = \frac{1}{2}\rho v^2 C_D A + fW + W\sin\,\theta, \text{ (83)}$$

where the first part is aerodynamic drag, the second part is the rolling resistance force and the third part is the climbing force. M is the vehicle full loading mass and the effective mass. The equivalent mass of the rotating components M_r can be obtained from the following equation:

$$M_r = M(1 + 0.04N_t N_f + 0.0025N_t^2 N_f^2) - M \text{ (84)}$$

N_t and N_f are the gear ratios for the final drive (differential) and transmission.

The following notations are introduced before we discuss the vehicle operation modes: SOC denotes the state of charge (SOC) in the battery-pack; $\dot{W}_{req}$ is the required road-load power; $\dot{W}_{fric}$ is the power dissipated by friction brakes; η_f is the differential efficiency; η_t is the transmission efficiency; η_m is the motor drive efficiency; $\dot{W}_{engine}$ is the engine's output power; and $\dot{W}_{motor}$ is the SPM motor's output power.

Based on the power distribution between SPM motors and ICE, the following diesel-HEV operation modes are defined and applied for computer simulation studies. The power management logic governs different vehicle operation modes to achieve the power boosting during acceleration, and regenerative braking during deceleration.

- Pure electric vehicle (PEV) mode: When the required road-load power is positive $\dot{W}_{req} > 0$, and the SOC is greater than a preset maximum threshold value SOC_{max}, i.e. $SOC > SOC_{max}$, the vehicle is completely driven by SPM motors and operated as a pure electric vehicle. Hence, when the battery is close to fully charged, the engine is shut off, the vehicle is operated as a PEV. The power required at the propeller shaft $\frac{\dot{W}_{req}}{\eta_f}$ equals to the power delivered to the propeller shaft by traction motors.

$$\frac{\dot{W}_{req}}{\eta_f} \text{ (85)}$$

- Power boost mode: When the required road-load power $\dot{W}_{req} > 0$, given battery state of charge is greater than a preset minimum threshold value SOC_{min}, but is less than a preset maximum threshold value, i.e., $SOC_{max} > SOC > SOC_{min}$, the following equation holds

$$\frac{\dot{W}_{req}}{\eta_f} = \eta_t \dot{W}_{engine} + \eta_m \dot{W}_{motor} \quad (86)$$

- The power required at the propeller shaft equals to the power delivered to the propeller shaft by the engine and SPMs, which is $\eta_t \dot{W}_{engine} + \eta_m \dot{W}_{motor}$.
- Pure ICE mode: When $\dot{W}_{req} \geq 0$ and the battery needs to be charged $SOC < SOC_{min}$, the HEV is operated in all ICE mode. Thus, we have

$$\frac{\dot{W}_{req}}{\eta_f} = \eta_t \dot{W}_{engine} \quad (87)$$

- Regenerative braking mode: When the vehicle is decelerating or declining a hill, the vehicle kinetic energy can be stored by operating the motor in the generator mode for recharging the battery. Under this condition, engine is shut off, and $\dot{W}_{req} \leq 0$. The power delivered to propeller shaft by the differential $\dot{W}_{req}\eta_f$ satisfies

$$\eta_f \dot{W}_{req} = \frac{\dot{W}_{motor}}{\eta_m} + \dot{W}_{fric} \quad (88)$$

The computer simulation results for heavy-duty diesel hybrid electric vehicle (HEV) are summarized in this section. To demonstrate the effectiveness of the proposed field oriented sliding mode control (FOSMC) in vehicle motion control applications. Fig. 13 shows the first-order and higher-order field oriented sliding mode control based diesel-HEV track the scheduled speed for the entire drive cycle. Fig. 14 show the zoomed-in view of HEV speed response comparisons. It is found that the higher-order FOSMC (labeled as "HOSM", and shown in red dash-dot line) tracks the reference speed (labeled as "REF", and shown in black dashed line) more closely than the first-order FOSMC approach (labeled as "FOSM", and shown in blue solid line) throughout the entire drive cycle.

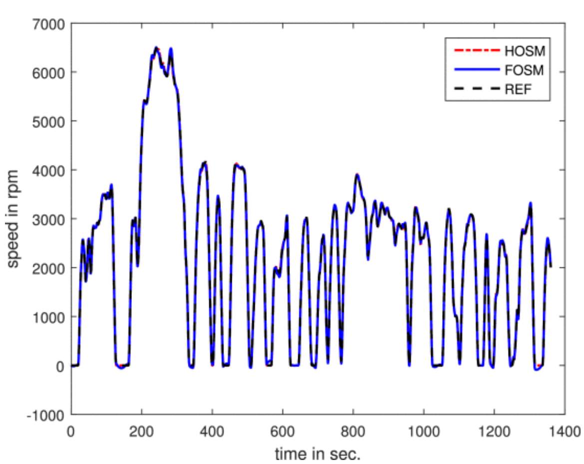

Fig. 13. Diesel hybrid electric vehicle speed response in rpm.

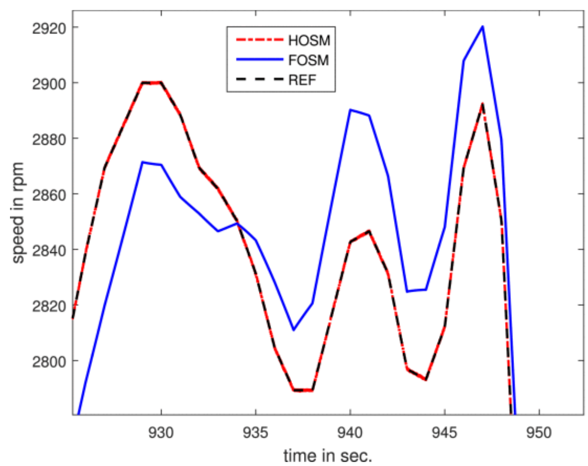

Fig. 14. Zoomed-in view of the vehicle speed response in rpm.

Fig. 15 shows the internal combustion engine's torque response. Fig. 16 shows the required vehicle power, the power from internal combustion engine, and the power from permanent magnet traction motors.

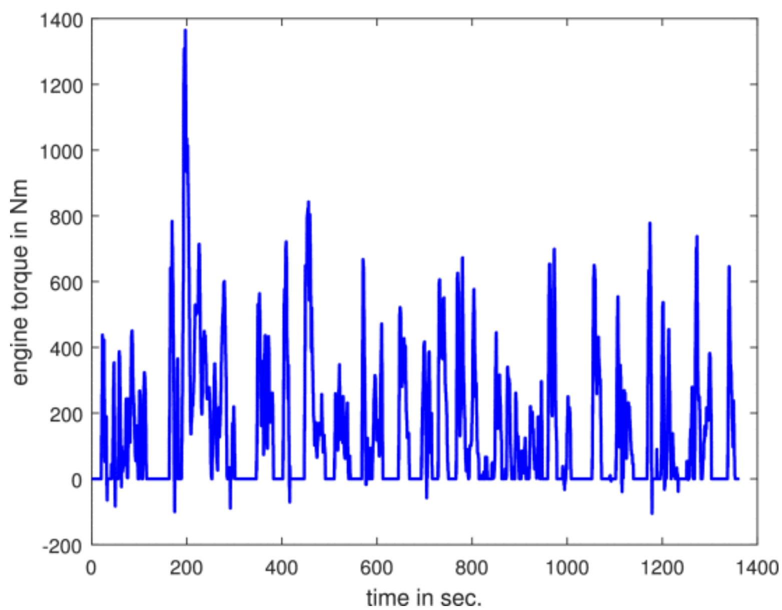

Fig. 15. Internal combustion engine torque response.

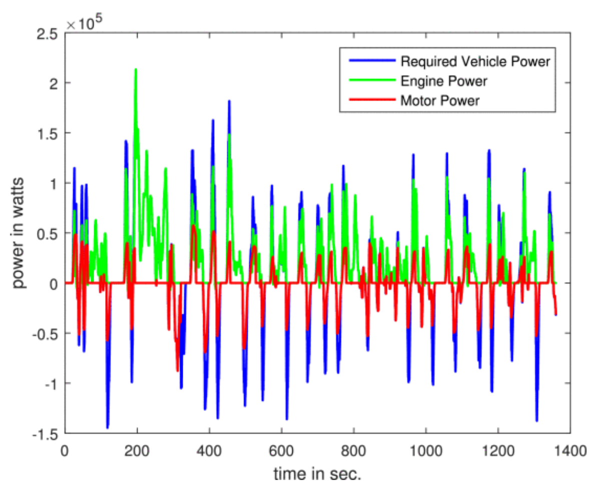

Fig. 16. Vehicle required power, engine power and motor power.

Fig. 17 and Fig. 18 compare the quadrature-axis stator current i_q 's responses based on the first-order and higher-order field oriented sliding mode control approaches, respectively. Noted that the -axis stator current i_q is proportional to the developed motor torque for SPM motors. It can be found that chattering is much more pronounced in the first-order FOSMC's iq response.

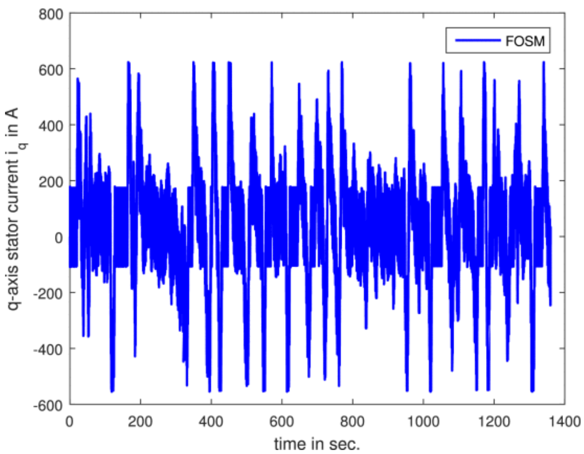

Fig. 17. Quadrature-axis stator current using the first-order FOSMC.

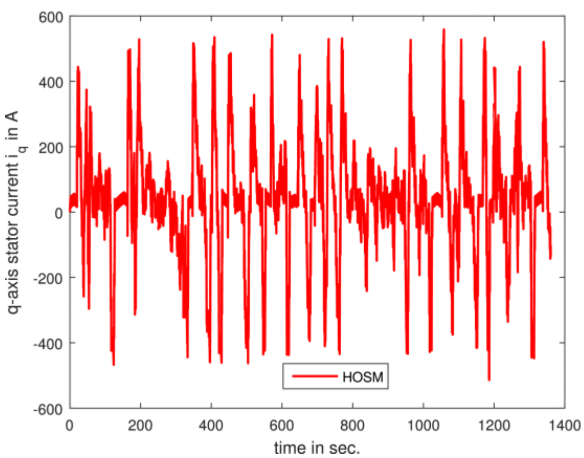

Fig. 18. Quadrature-axis stator current using the higher-order FOSMC.

Similarly, the direct-axis stator current i_d responses are summarized in Fig. 19 and Fig. 20. Fig. 19 is based on the first-order field oriented sliding mode control approach, and Fig. 20 is based on the higher-order approach. i_d is successfully regulated to be 0, in order to maximize the developed electromechanical torque of the PM traction motors. Again, chattering is much more noticeable in the first order FOSMC's i_d response.

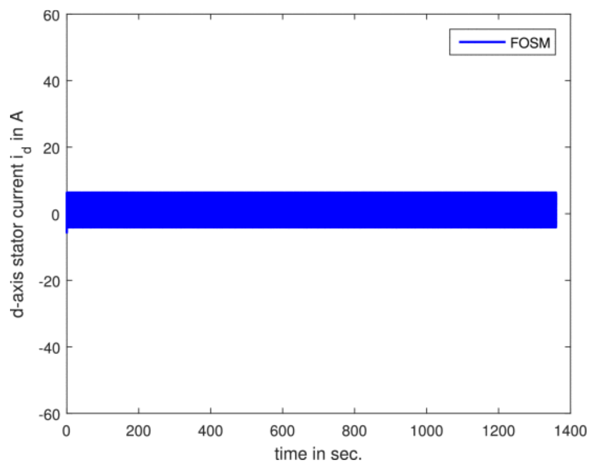

Fig. 19. Direct-axis stator current using the first-order FOSMC.

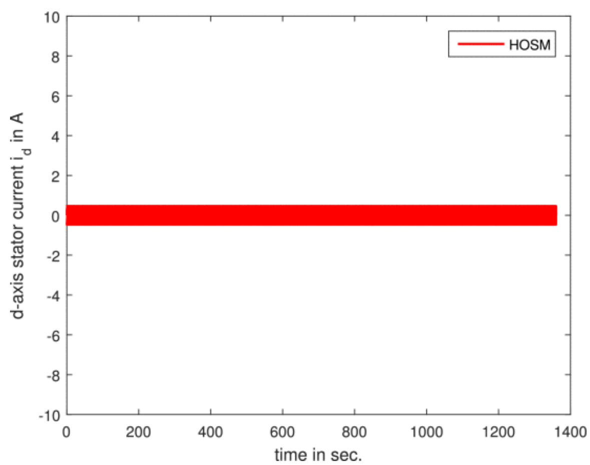

Fig. 20. Direct-axis stator current using the higher-order FOSMC.

Lastly, Fig. 21 and Fig. 22 compare the developed electromechanical torque response from each SPM traction motor by using the first-order and higher-order field oriented sliding mode control, respectively. The first-order field oriented sliding mode control shows conspicuous chattering, while the higher-order field-oriented sliding mode greatly reduces the chattering in torque response.

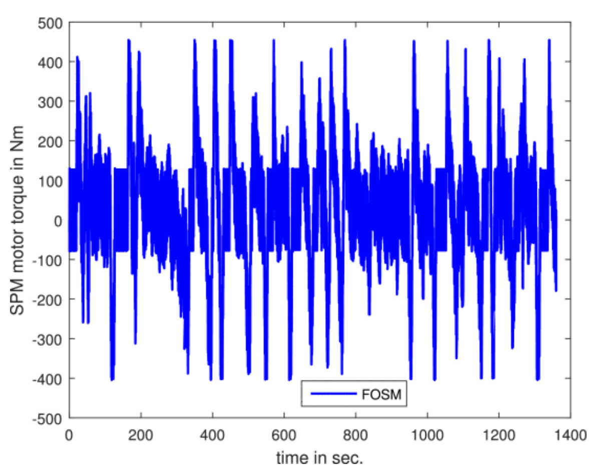

Fig. 21. SPM traction motor torque response using the first-order FOSMC.

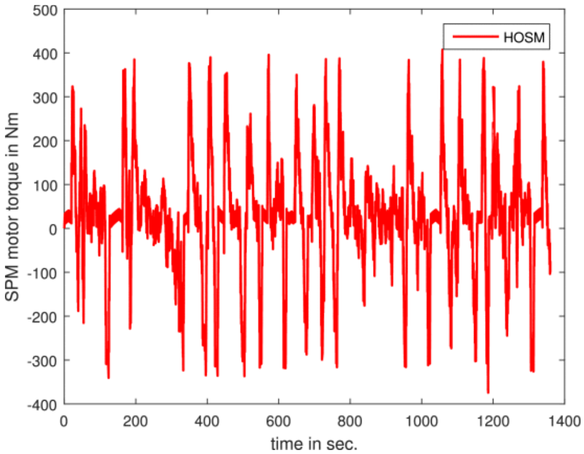

Fig. 22. SPM traction motor torque response using the higher-order FOSMC.

SECTION VIII. Conclusion

This paper has proposed the novel theory, design, simulation and implementation of both first- and higher-order field oriented sliding mode control (FOSMC) of surface-mounted permanent magnet AC motors with applications to electrified vehicles. Hardware experimental results and computer simulation studies have demonstrated that the higher-order sliding mode controller is superior to the first-order scheme by offering a faster transient response and eliminating the chattering phenomenon. Furthermore, the proposed field oriented sliding mode control methods have also been successfully applied in permanent magnet traction motor control of a heavy-duty diesel hybrid electric vehicle tested under UDDS urban driving schedule.

Abstract:

Permanent magnet ac motors have been extensively utilized for adjustable-speed traction motor drives, due to their inherent advantages including higher power density, superior efficiency and reliability, more precise and rapid torque control, larger power factor, longer bearing, and insulation life-time. Without any proportional-and-integral (PI) controllers, this paper introduces novel first- and higher-order field-oriented sliding mode control schemes. Compared with the traditional PI-based vector control techniques, it is shown that the proposed field oriented sliding mode control methods improve the dynamic torque and speed response, and enhance the robustness to parameter variations, modeling uncertainties, and external load perturbations. While both first- and higher-order controllers display excellent performance, computer simulations show that the higher-order field-oriented sliding mode scheme offers better performance by reducing the chattering phenomenon, which is presented in the first-order scheme. The higher-order field-oriented sliding mode controller, based on the hierarchical use of supertwisting algorithm, is then implemented with a Texas Instruments TMS320F28335 DSP hardware platform to prototype the surface-mounted permanent magnet ac motor drive. Last, computer simulation studies demonstrate that the proposed field-oriented sliding mode control approach is able to effectively meet the speed and torque requirements of a heavy-duty electrified vehicle during the EPA urban driving schedule.

Published in: IEEE Transactions on Vehicular Technology (Volume: 67 , Issue: 11 , Nov. 2018)

Page(s): 10343 - 10356

Date of Publication: 17 August 2018

ISSN Information:

INSPEC Accession Number: 18219054

DOI: 10.1109/TVT.2018.2865905

Publisher: IEEE

SECTION I.

Introduction and Motivation

Thanks to the latest development of AC electric motors and battery technologies, a wide range of electrified vehicles hit the production line and become commercially available. From the rise of electrified heavy-duty trucks, such as Tesla Semi-truck, to the huge market growth of passenger-type hybrid electric vehicles, such as Toyota Prius, the future of transportation industry and market will be dominated by all types of electrified vehicles, including pure electric vehicles (PEVs), hybrid electric vehicles (HEVs), and fuel-cell vehicles (FCVs).

Besides reduction of the carbon dioxide emission and high energy efficiency, the three distinct advantages of electrified vehicles have been summarized by Hori in [1] as follows:

1. *Precise and fast toque generation from electric motors:* The electric motor's torque response is typically within several milliseconds, whereas the response of an internal combustion engine or a hydraulic braking system is 10 to 100 times slower. Utilizing this essential feature, advanced control of traction motors enables dynamically changing the vehicle's characteristics without changing the driver's behavior. Anti-lock braking system (ABS) and traction control system (TCS) can be cooperated and integrated together, since motor can produce both acceleration and deceleration torques. Battery energy savings can be optimized by using regenerative braking and low-drag tires.
2. *A motor can be attached to each wheel:* Toque from smaller-sized motor-wheel sets can be controlled independently and cooperatively, which leads to safety and performance improvements of electrified vehicles. Distributed motor location can enhance the performance of vehicle stability control (VSC), which is not achievable in traditional internal combustion engine (ICE) based vehicles.
3. *Motor torque can be easily measured:* The driving and braking torque generated from electric motors enjoys much smaller uncertainties, compared to that of an IC engine or hydraulic brake. Based upon current measurement, driving force observer can be developed to estimate the driving and braking force between tire and road in real-time, which enables control technologies to safely governs the vehicle traction based on road condition estimation.

For aforementioned electrified vehicles traction control, adjustable speed permanent magnet AC motor (PMAC) drives have been extensive employed. As an example, the 8-pole interior-mounted permanent magnet AC motors (IPMs) are commonly used in Toyota Prius for traction and regenerative braking. The popularity of poly-phase permanent magnet AC motors should be attributed to their inherent advantages of more accurate and faster torque control, larger torque to inertia ratio, higher power density, longer bearing and insulation life-time, larger power factor, superior efficiency and reliability, when compared to other types of electric motor drives.

Over the past decades, the vast majority of academic and industrial effort approaches high performance real-time PMAC motor control challenge by means of *field oriented control* (FOC) and *direct torque control* (DTC) [2], also known as vector control. Without the large current harmonics or torque ripples inherent in direct torque control [3]- [6], field oriented control is traditionally executed through proportional-integral (PI) controllers. Although a PI controller enjoys the advantage of simplicity and the ease of implementation, its design process suffers from the following distinct drawbacks:

1. A PI controller may not provide satisfactory transient performance, since it does not take *load perturbations, external disturbances, parameters variations and modeling uncertainties* into account. Therefore, a PI controller is not a very robust linear controller.

2. In order to design PI-based field oriented controllers, *decoupling system is needed to convert the nonlinear PM motor dynamics into classical single-input-single-output (SISO) systems*, so that PI control gain can be computed based on the chosen phase and gain margins to meet the stability requirements of linear control. Discrepancies between the actual nonlinear PMAC motor dynamics and the linear SISO models employed for PI controller design deteriorate the field oriented control performance, in which the stability of closed-loop feedback AC motor control systems is also compromised.

Actually, in additional to coupled nonlinearities, permanent magnet synchronous motor drives face with parameter variations, modeling uncertainties and extraneous load perturbations. Unfortunately, conventional linear control approaches, including aforementioned proportional-integral (PI) approach and linear quadratic regulator (LQR) method cannot achieve sufficiently high performance for permanent magnet AC motor systems due to the inherent limitations. Hence, a high performance nonlinear control scheme would be desirable to overcome these difficulties in practical electrified vehicle applications, which guarantees fast and stable transient behavior, quick toque and speed recovery from disturbances and perturbations, and robustness against system parameter variations and modeling uncertainties.

To address this application-oriented challenge, many nonlinear control methods have been recently developed as compelling alternatives to classical PI controllers. These nonlinear controls include fuzzy control, robust control, state dependent Riccati equation based control, model predictive control, feed-forward control, adaptive control, intelligent control, neural-network control, feedback linearization, and sliding mode control, which have been studied and reported in literature [7]–[32] . In [7], the fuzzy control methods have limitations to choose the appropriate membership functions and fuzzy rules for the fuzzy inference motion control system. Robust control, such as $H\infty$ control method in [8], requires complicated design processes and much more complicated numerical solvers to compute the control solution. The state dependent Riccati equation control requires the solutions from Riccati equation at each time-step [9], [10] . If the Riccati equation solution is infeasible, then the motor control is failed. In [11], model predictive control (MPC) can provide good performance in instantaneous current control for motor drive, but MPC is not robust. An intelligent control or a neural network-based control technique requires a huge amount of computation complexity, while its control performance is not guaranteed, and there is no stability warranty [12], [13]. Linear quadratic regulator (LQR) based optimal vector control of PMSM in dq synchronous coordinate frame with state feedback is reported in [14]. However, LQR optimal control is designed for torque and speed regulation around the steady-state operating point. Furthermore, LQR control is not robust, and can be sensitive to model uncertainties, external disturbances and extraneous noise. [15] proposes a modified vector-controlled IPM drive system with the purpose of minimizing copper losses based upon a voltage-constrained tracking in the field weakening control. The approach is designed based on steady state voltage equations, i.e. the time derivatives of currents are ignored. [16] presents a combined adaptive control, fuzzy logic, neural network and genetic algorithm based control of a linear induction motor drive, which is complicated to be implemented in practice, and without stability guarantee. Different from the feedback linearization method used in [17], [18] applies the Hamiltonian of nonlinear optimal control theory to achieve the feedback linearization control of PM synchronous machines operating with varying speed/torque. Feedback linearziation requires transformation must be a diffeomorphism, i.e., the transformation must be invertible. But in practice, the transformation of motor model can only be locally diffeomorphic, the feedback linearziation results only hold within a small neighborhood of equilibrium point, therefore, the method in [18] also have limitations for practical motor-drive applications.

It should be mentioned the Maximum Torque Per Ampere (MTPA) control technique has been widely utilized as a practical interior-mounted permanent magnet synchronous motor (IPM) motion control solution [19]–[23]. For a given magnitude of current vector, the stator current vector can be controlled using MTPA control to maximize the developed torque. The MTPA method has been extensively used, as it can be conveniently implemented with PI controllers, while minimizing the copper loss. However, MTPA cannot be applied above the rated speed due to the voltage limit. [19] proposes the high-performance current regulator to improve current responses in high-speed flux-weakening region by a feed-forward compensator. This control strategy has been widely adopted in constant torque operating range to achieve fast transient and high-efficiency operation of IPM drive systems.

Sliding modes are well-known for their robustness against parameter variations, modeling uncertainties, external disturbances and perturbations in the mathematical description of physical systems [24]-[32]. Compared with a proportional-integral (PI) controller, a sliding mode scheme improves the dynamic performance, reduces the response-time and overshoot, provides perfect decoupling, and enhances the overall stability of permanent magnet AC motor drives.

Extending our previous effort in [33], [34], where we focus on first and higher-order sliding mode theory development, this manuscript presents novel first and higher-order *field oriented sliding mode control* strategies to develop high performance surface-mounted permanent magnet AC motor drives (SPMs) operating smoothly and robustly over the full-speed range, with the maximized electromechanical torque output. The main contributions of this manuscript are summarized as follows:

1. The proposed *field oriented sliding mode control* scheme (FOSMC) enjoys the combined advantages of field oriented control and sliding mode control. On the one hand, the field oriented control scheme maximizes the developed electromechanical torque by setting the flux and stator current vectors orthogonal with each other, since the developed electromechanical torque can be expressed as the outer product of the two vectors. On the other hand, the sliding mode control scheme can guarantee faster transient behavior, less overshoot, smaller steady state error, less sensitive to model parameter variations and load torque perturbations, when compared to PI or LQR based linear controllers.

2. This manuscript approaches the chattering problem by utilizing the novel higher-order FOSMC control method based on the hierarchical use of the super-twisting algorithm. The ideal property of super-twisting algorithm (STA) is that it does not require any time-derivatives of the sliding variables.

3. To confirm the effectiveness and robustness of the proposed field oriented sliding mode control, experiments are carried out with computer simulations and hardware implementations involving a Texas Instruments TMS320F28335 DSP based prototype platform.

4. A heavy-duty hybrid electric vehicle is modeled and controlled with the proposed higher-order sliding mode controller. The EPA Urban Dynamometer Driving Schedule (UDDS) is used for the reference test-

drive input to the vehicle. Simulation studies verify that the proposed controller is able to nearly perfectly track the speed reference.

The remainder of this manuscript is structured as follows: Section II establishes the dynamic modeling of surface-mounted permanent magnet synchronous motors. The proposed field oriented sliding mode control scheme is introduced and compared with the traditional proportional-integral (PI) based field oriented control scheme. Section III presents the overview of sliding mode control theory. Section IV gives the detailed derivation of the first-order field oriented sliding mode controller. Section V presents the detailed design of the higher-order sliding mode controller. The implementation of Texas Instruments TMS320F28335 DSP based platform are summarized in Section VI. Section VII provides the modeling of hybrid electric vehicle, and numerical simulation of hybrid electric vehicle controlled with the field-oriented sliding mode control under the UDDS driving cycle. Finally, we conclude the paper in Section VIII by highlighting directions for future work.

SECTION II.

Dynamics of Surface-Mounted Permanent Magnet AC Motors

Consider the dq synchronous frame model of a 3-phase surface-mounted permanent magnet synchronous motor (SPM) given as [35] :

$$\frac{di_d}{dt}=-\frac{R_s}{L}i_d+\frac{P}{2}\omega_r i_q+\frac{1}{L}u_d \tag{1}$$

View Source

$$\begin{aligned}\frac{di_q}{dt}&=-\frac{R_s}{L}i_q-\frac{P}{2}\omega_r i_d-\frac{\frac{P}{2}\omega_r\Phi_m}{L}+\frac{1}{L}u_q \qquad (2)\\ \frac{d\omega_r}{dt}&=\frac{\tau_e}{J}-\frac{\tau_m}{J}-\frac{B\omega_r}{J}, \qquad (3)\end{aligned}$$

View Source where u_d and u_q are the stator voltage component defined in dq synchronous reference frame; i_d and i_q are the stator current components defined in dq synchronous reference frame; ω_r is the rotor speed in mechanical rad/sec.; P is the number of poles; Φ_m is the permanent magnet rotor flux linkage; J is the rotor moment of inertia; B is the viscous damping coefficient; τ_m is the load torque; R_s is the armature winding resistance; and L is the stator inductance. The developed electromechanical torque τ_e can be expressed as:

$$\tau_e=\frac{3P}{4}\Phi_m i_q \tag{4}$$

View Source It should be noted that for SPM, there is no reluctance torque component existed in (4), since the direct- and quadrature-axis stator inductances are the same, i.e., $L_d=L_q=L$.

Notice that motor dynamics (1)– (3) are cross-coupled nonlinear equations. For traditional field oriented control scheme, the development of proportional-integral (PI) based controllers requires decoupling and back-emf compensation as shown in (6). Decoupling systems are essential to convert the nonlinear coupled dynamics into single-input-single-output linear models. By performing the decoupling stage as shown in Fig. 1, the two inputs to space-vector pulse-width-modulation scheme, u_d and u_q, can be expressed as

$$\begin{aligned}u_d&=(PI)(i^*_d-i_d)-\frac{P}{2}\omega_r L i_q \qquad (5)\\ u_q&=(PI)(i^*_q-i_q)+\frac{P}{2}\omega_r L i_d+\frac{P}{2}\omega_r\Phi_m \qquad (6)\end{aligned}$$

View Source where PI stands for a standard proportional-integral controller.

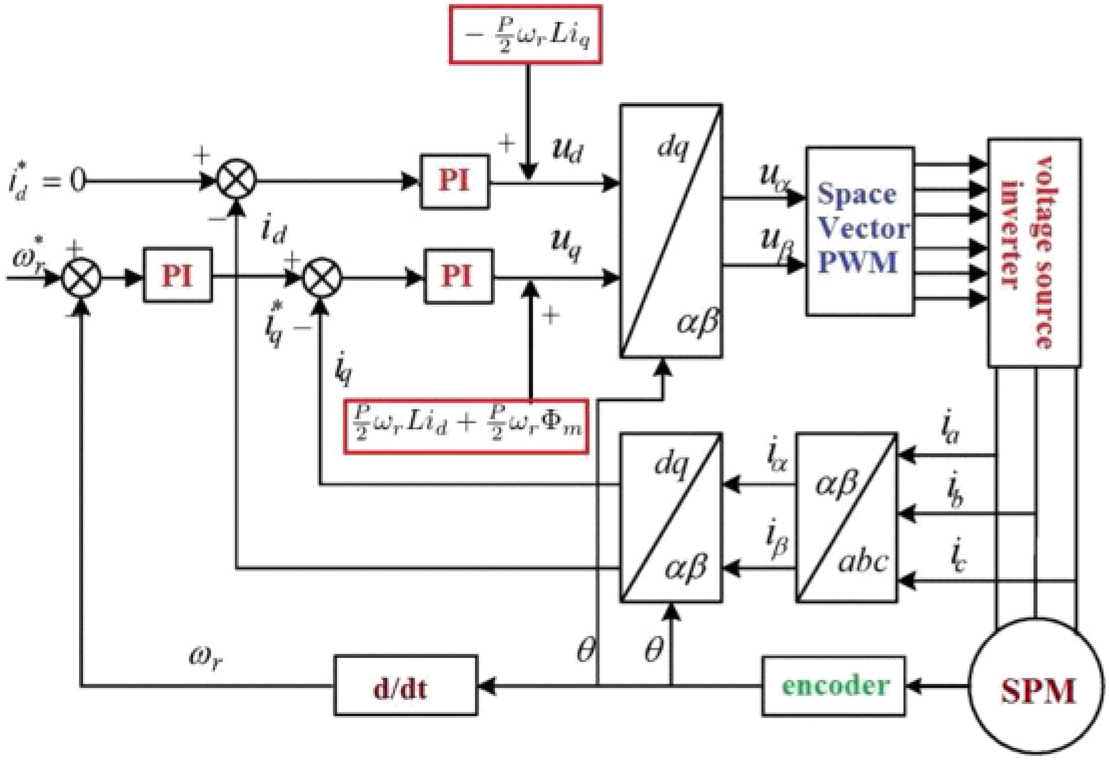

Fig. 1.

Block diagram of the traditional proportional-integral based field oriented control.

View All

Different from the traditional PI-based field oriented scheme, the proposed field-oriented sliding mode control of surface-mounted permanent magnet AC motors (SPMs) does not involve any decoupling blocks as shown in Fig. 2. With the measurement feedback of id, iq , ωr, the proposed field oriented sliding mode control can be achieved by implementing velocity sliding mode controller, flux sliding mode controller and torque sliding mode controller. The orthogonality of flux and current space vectors are guaranteed by aligning the armature current vector along the q-axis, i.e., i∗d=0, and the flux vector along the d-axis. An encoder or resolver-to-digital converter (RDC) can provide the mechanical rotor position θr and speed ωr information in real-time as shown in Fig. 2.

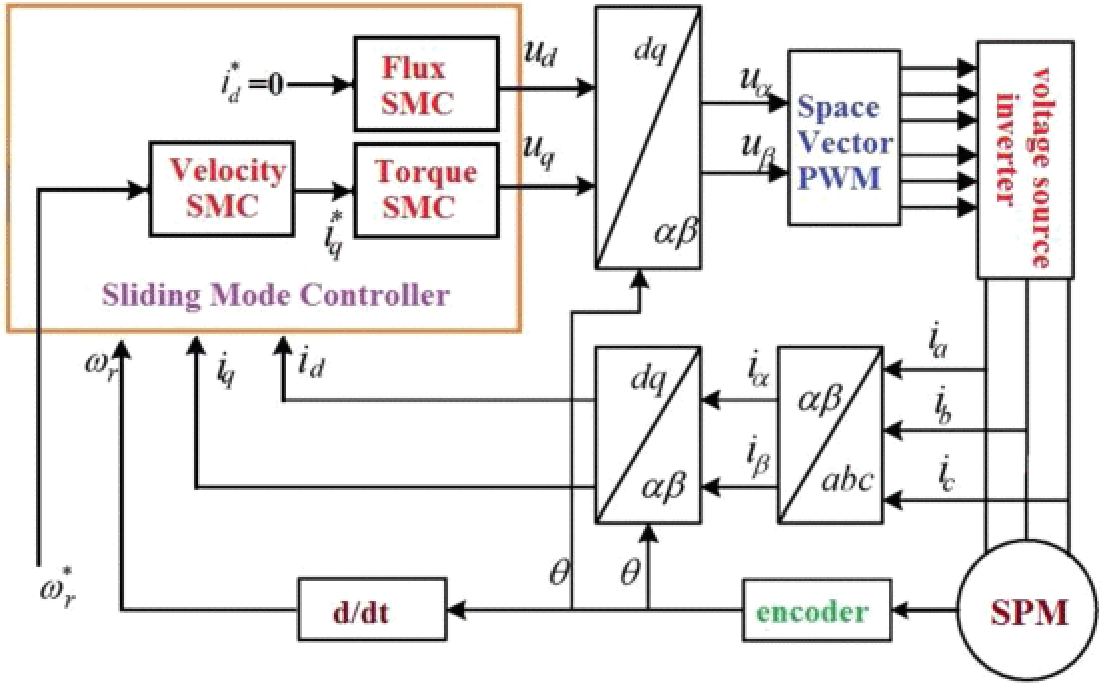

Fig. 2.

Block diagram of the proposed field oriented sliding mode control.

View All

SECTION III.

Sliding Mode Control Theory

One of the most intriguing aspects of a sliding mode controller is that by utilizing a discontinuous control approach whose primary function is to rapidly switches between two distinct continuous manifolds, the controlled system dynamics is forced to track a predetermined trajectory known as the sliding surface [30], [31].

Consider the following input-affine nonlinear dynamics

$$\dot{x}(t)=f(x,t)+h(x,t)\cdot u(t), \quad (7)$$

View Source where $x\in R^n$ denotes the state-space variable. $f(x,t)$ and $h(x,t)$ are smooth $n\times n$ and $n\times m$ nonlinear vector functions, respectively. The discontinuous control input $u\in R^m$ is expressed as

$$u=\begin{cases} U^+(x,t) & \text{if } s(x)>0 \\ U^-(x,t) & \text{if } s(x)<0 \end{cases}, \quad (8)$$

View Source where $s(x)=(s_1(x),\dots,s_m(x))^T$ defines the sliding manifold, while $s_i(x)=0, \forall i=1\dots m$ describe the m sliding surfaces.

The aforementioned closed-loop control system exhibits sliding mode properties if the following reachability, existence, and stability conditions are satisfied:

1) *Reachability condition:* ensures that state trajectory will approach and eventually reach the sliding manifold, by satisfying the following condition:

$$s(x,t)\dot{s}(x,t)<0 \tag{9}$$

View Source

2) *Existence condition:* guarantees that once state trajectory is within the neighborhood of sliding manifold, it will be directed toward the sliding surface, by meeting the following requirement:

$$\lim_{s\to 0} s(x,t)\dot{s}(x,t)<0 \tag{10}$$

View Source

3) *Stability condition:* secures that the sliding manifold will direct the state trajectory toward the stable equilibrium point, which can be obtained by checking the stability in steady-state.

Now, we are in the position to describe the main results, which provide optimal and robust solutions for the field oriented sliding mode control of a surface-mounted permanent-magnet synchronous motor.

A. Sliding Surfaces

The sliding manifold $s(x,t)=(s_d,s_q,s_{\omega r})^T$ of the field-oriented sliding mode control is governed by

$$\begin{aligned} s_d &= i_d - i_d^* = 0 && (11)\\ s_q &= i_q - i_q^* = 0 && (12)\\ s_{\omega r} &= \omega_r - \omega_r^* = 0 && (13) \end{aligned}$$

View Source

B. Parameter Uncertainties

Considering modeling uncertainties, unmodeled dynamics, and parameter variations in the permanent magnet AC motor dynamics, the following notations are introduced: $R_s=\hat{R}_s+\Delta R_s$; $L=\hat{L}+\Delta L$; $\Phi_m=\hat{\Phi}_m+\Delta\Phi_m$; $\tau_m=\hat{\tau}_m+\Delta\tau_m$; $J=\hat{J}+\Delta J$; and $B=\hat{B}+\Delta B$. Note that $\hat{\cdot}$ denotes the nominal value, and $\Delta\cdot$ denotes the bounded parameter uncertainty/variation.

SECTION IV.

First-Order Sliding Mode Control Design

A. First-Order Flux Sliding Mode Control

The d-axis magnetic-flux control law is given as

$$u_d=u_{d,eq}+u_{d,N} \tag{14}$$

View Source where u_d is the direct-axis stator voltage, $u_{d,eq}$ is the equivalent control and $u_{d,N}$ is the switching control.

The equivalent control can be obtained from $\dot{s}_d=0$.

$$\dot{s}_d=\frac{1}{L}\left[-R_s i_d+\frac{P}{2}\omega_r L i_q+u_d-L\frac{di_d^*}{dt}\right] \tag{15}$$

View Source

Solving for ud,eq results in

ud,eq=R^sid−P2wrL^iq+L^di∗ddt(16)

View Source

Equivalently, s˙d in (15) can be represented as

s˙d=1L[−ΔRid+P2ωrΔLiq+ud,N−ΔLdi∗ddt](17)

View Source

Based upon LaSalle's invariance principle, we can obtain the switching control component guaranteeing the Lyapunov stability. Since the uncertainties present in the parameters are bounded, there exists a positive upper-bound ud0, such that

ud0>∣∣∣ΔRid+ΔLdi∗ddt−P2ωrΔLiq∣∣∣(18)

View Source The switching control component of ud is then obtained as

ud,N=−ud0sgn(sd),(19)

View Source where the signum function sgn() is known as

sgn(s)=⎧⎩⎨⎪⎪10−1if s>0if s=0if s<0(20)

View Source

B. First-Order Torque Sliding Mode Control

The q-axis torque control law is given as:

uq=uq,eq+uq,N,(21)

View Source where uq is the quadrature-axis stator voltage, uq,eq is the equivalent control and uq,N is the switching control.

Using the aforementioned method, we first derive s˙q to be

s˙q=1L[−Rsiq−P2ωrΦm−P2ωrLid+uq−Ldi∗qdt](22)

View Source

The q-axis equivalent control can be obtained as follows

uq,eq=R^siq+P2ωrL^id+P2ωrΦ^m+L^di∗qdt(23)

View Source s˙q is then rewritten as

s˙q=1L[−ΔRiq−P2ωrΔΦm−P2ωrΔLid+uq,N−ΔLdi∗qdt](24)

View Source

Similarly, since the parameter uncertainties are all bounded, there exists a positive upper-bound uq0, such that

uq0>|||ΔRiq+P2ωrΔLid+P2ωrΔΦm+ΔLdi∗qdt|||(25)

View Source The switching control component of uq is then obtained as

uq,N=−uq0sgn(sq)(26)

View Source

The q-axis torque control action keeps iq converging to the desired reference q-axis stator current i∗q.

C. First-Order Velocity Sliding Mode Control

We define the q-axis velocity control law as

i∗q=i∗q,eq+i∗q,N,(27)

View Source where iq is the quadrature-axis stator current, iq,eq is the equivalent control and iq,N is the switching control.

From the sliding surface sωr, s˙ωr is found to be

s˙ωr=3PΦm4Jiq−τmJ−BωrJ−dω∗rdt(28)

View Source

The equivalent control becomes:

i∗q,eq=1Kt[τ^m+B^ωr+J^dω∗rdt],(29)

View Source where

Kt=34PΦm.(30)

View Source

Following the similar procedure as the previous control designs, there exists a positive upper-bound iq0, such that

iq0>|||1Kt(Δτm+ΔBωr+ΔJdω∗rdt)|||(31)

View Source

The switching control component of i∗q is then obtained as

i∗q,N=−iq0sgn(sωr)(32)

View Source

The output of q-axis velocity control, i∗q, serves as the input to q-axis torque sliding mode control in Section IV Part B.

SECTION V.

Higher-Order Sliding Mode Control Design

The oscillatory dynamic behavior about the sliding manifold, commonly known as chattering, exists in the first-order sliding mode scheme. Chattering effect, which is caused by the imperfections of switching devices, is the major drawback of the first-order approach. To eliminate the chattering phenomenon, the second-order sliding mode control methods is developed using the super-twisting algorithm (STA). Some preliminary results on higher-order sliding mode control are given in [30]. Sliding manifolds s for higher-order sliding modes are chosen to be the same as the first-order sliding manifolds. Therefore, the equivalent controls for higher-order sliding modes are the same ones for first-order sliding modes. STA can be summarized as follows:

Let $y_1=s$, $y_2=\dot{s}$, then

$$\begin{aligned} \dot{y}_1 &= y_2 = \dot{s} = \frac{\partial s}{\partial t} + \frac{\partial s}{\partial x}\dot{x} \\ \dot{y}_2 &= \ddot{s} = \left(\frac{\partial \dot{s}}{\partial t} + \frac{\partial \dot{s}}{\partial x}\dot{x}\right) + \frac{\partial \dot{s}}{\partial u}\dot{u} = \psi(x,t) + \gamma(x,t)\dot{u} \end{aligned} \tag{33}$$

View Source where

$$|\psi| \le \Psi, \quad \Psi > 0, \quad 0 < \Gamma_m \le \gamma \le \Gamma_M, \tag{34}$$

View Source with the lower-bound and the upper-bound of γ denoted as Γ_m and Γ_M, respectively.

The switching control algorithm is defined by the following control law:

$$\tilde{u} = u_1 + u_2 \tag{35}$$

View Source with

$$\begin{aligned} \dot{u}_1 &= -W \operatorname{sgn}(y_1) \quad (36) \\ u_2 &= \begin{cases} -\lambda |s_0|^p \operatorname{sgn}(y_1) & |y_1| > |s_0| \\ -\lambda |y_1|^p \operatorname{sgn}(y_1) & |y_1| \le |s_0| \end{cases}, \quad (37) \end{aligned}$$

View Source where W, λ, p are positive sliding mode constants. The corresponding sufficient conditions for finite-time convergence to the sliding surface are given as follows:

$$\begin{aligned} W &> \frac{\Psi}{\Gamma_m} \quad (38) \\ \lambda^2 &\ge \frac{4\Psi \Gamma_M (W+\Psi)}{\Gamma_m^2 \Gamma_m (W-\Psi)} \quad (39) \\ 0 &< p \le 0.5 \quad (40) \end{aligned}$$

View Source

The distinct advantage of super-twisting algorithm (STA) is that it does not require any information of the time derivative of the sliding variables. It is noteworthy that this merit is essential for real-time hardware implementation of the proposed higher-order field oriented sliding mode control (FOSMC).

Also note that, by selecting $p=1$, the aforementioned control algorithm converges to the sliding surface exponentially, which leads to an exponentially stable 2-sliding mode in the sense of Lyapunov. The selection of $p=0.5$ ensures that the maximal possible for 2-sliding realization real-sliding order 2 is achieved.

A. Higher-Order Flux Sliding Mode Control

For second-order sliding mode control, both $s(x)$ and $\dot{s}(x)$ are set to be zero. From the Section IV part A results on $\dot{s}_d$

$$\dot{s}_d = \frac{1}{L}\left[-R_s i_d + \frac{P}{2}\omega_r L i_q + u_d - L\frac{d i_d^*}{dt}\right] \tag{41}$$

View Source $\ddot{s}_d$ is obtained by taking derivative of (41) as s¨d=−RsLdiddt+P2dωrdtiq+P2diqdtωr+1Lduddt−d2i∗ddt(42)

View Source Denote

ψd=−RsLdiddt+P2dωrdtiq+P2diqdtωr−d2i∗ddt∈[−Ψd,Ψd](43)

View Source and

γd=1L∈[Γmd,ΓMd](44)

View Source

Denoting ζL=|ΔL|≪L^, we may choose the lower- and upper-bound Γmd,ΓMd as follows

ΓmdΓMd=1L^+ζL>0,=1L^−ζL>0(45)(46)

View Source

Control input ud consists of the sum of equivalent control ud,eq and switching control u~d. Note that the equivalent control ud,eq is the same as (16), and the switching control u~d is given as:

u~d=ud1+ud2(47)

View Source with

u˙d1ud2=−Wdsgn(sd)={−λd|s0|psgn(sd)−λd|sd|psgn(sd)|sd|>|s0||sd|≤|s0|(48)(49)

View Source

The sufficient conditions for finite-time convergence to the sliding surface are summarized as follows:

Wdλ2d0>ΨdΓmd≥4ΨdΓ2mdΓMd(Wd+Ψd)Γmd(Wd−Ψd)<p≤0.5(50)(51)(52)

View Source

We choose p=0.5 in this manuscript for implementing the proposed higher-order sliding mode control. The controller can be simplified by selecting s0=∞. Therefore, we have

u~d=−λd|sd|1/2sgn(sd)−Wd∫sgn(sd)dt(53)

View Source

B. Higher-Order Torque Sliding Mode Control

The similar method used for the d-axis flux control is applied for developing the q-axis torque sliding mode control. Based on previous analysis in Section IV Part B, s˙q is expressed as

s˙q=1L[−Rsiq−P2ωrΦm−P2ωrLid+uq−Ldi∗qdt](54)

View Source

By taking the second-order derivative, s¨q can be obtained as

$$\ddot{s}_q = -\frac{R_s}{L}\frac{di_q}{dt} - \frac{P}{2}\omega_r\frac{di_d}{dt} - \frac{P}{2}i_d\frac{d\omega_r}{dt} - \frac{P}{2}\frac{\Phi_m}{L}\frac{d\omega_r}{dt} + \frac{1}{L}\frac{du_q}{dt} - \frac{d^2 i^*_q}{dt^2} \tag{55}$$

View Source

Denote

$$\psi_q = -\frac{R_s}{L}\frac{di_q}{dt} - \frac{P}{2}\omega_r\frac{di_d}{dt} - \frac{P}{2}i_d\frac{d\omega_r}{dt} - \frac{P}{2}\frac{\Phi_m}{L}\frac{d\omega_r}{dt} - \frac{d^2 i^*_q}{dt^2} \in [-\Psi_q, \Psi_q] \tag{56}$$

View Source and

$$\gamma_q = \frac{1}{L} \in [\Gamma_{mq}, \Gamma_{Mq}] \tag{57}$$

View Source

Similarly, denoting $\zeta_L = |\Delta L| \ll \hat{L}$, we may choose the lower- and upper-bound Γ_{mq}, Γ_{Mq} as follows

$$\Gamma_{mq} = \frac{1}{\hat{L}+\zeta_L} > 0, \tag{58}$$
$$\Gamma_{Mq} = \frac{1}{\hat{L}-\zeta_L} > 0 \tag{59}$$

View Source

Control input u_q consists of the sum of equivalent control $u_{q,eq}$ and switching control $\tilde{u}_q$.

$$u_q = u_{q,eq} + \tilde{u}_q \tag{60}$$

View Source

Note that the equivalent control $u_{q,eq}$ is the same as (23), and the switching control $\tilde{u}_q$ is given as

$$\tilde{u}_q = u_{q1} + u_{q2} \tag{61}$$

View Source

with

$$\dot{u}_{q1} = -W_q \operatorname{sgn}(s_q) \tag{62}$$

View Source

$$u_{q2} = \begin{cases} -\lambda_q |s_0|^p \operatorname{sgn}(s_q) & |s_q| > |s_0| \\ -\lambda_q |s_q|^p \operatorname{sgn}(s_q) & |s_q| \le |s_0| \end{cases} \tag{63}$$

View Source

The sufficient conditions for finite-time convergence to the sliding surface are summarized as follows

$$W_q > \frac{\Psi_q}{\Gamma_{mq}}, \tag{64}$$
$$\lambda_q^2 \ge \frac{4\Psi_q}{\Gamma^2_{mq}}\frac{\Gamma_{Mq}(W_q+\Psi_q)}{\Gamma_{mq}(W_q-\Psi_q)}, \tag{65}$$
$$0 < p \le 0.5 \tag{66}$$

View Source

The controller can be simplified by selecting $s_0 = \infty$. Hence, $\tilde{u}_q$ can be expressed as

$$\tilde{u}_q = -\lambda_q |s_q|^{1/2}\operatorname{sgn}(s_q) - W_q \int \operatorname{sgn}(s_q)\,dt \tag{67}$$

View Source

C. Higher-Order Velocity Sliding Mode Control

By applying similar methods, from the Section IV Part C, we have

$$\dot{s}_{\omega r}=\frac{3P\Phi_m}{4J}i_q-\frac{\tau_m}{J}-\frac{B\omega_r}{J}-\frac{d\omega^*_r}{dt} \tag{68}$$

View Source

Therefore, $\ddot{s}_{\omega r}$ is obtained by taking the second-order derivative of $s_{\omega r}$ as

$$\ddot{s}_{\omega r}=\frac{K_t}{J}\frac{di_q}{dt}-\frac{1}{J}\frac{d\tau_m}{dt}-\frac{B}{J}\frac{d\omega_r}{dt}-\frac{d^2\omega^*_r}{dt^2} \tag{69}$$

View Source

Again, denote

$$\psi_{\omega r}=-\frac{1}{J}\frac{d\tau_m}{dt}-\frac{B}{J}\frac{d\omega_r}{dt}-\frac{d^2\omega^*_r}{dt^2}\in[-\Psi_\omega,\Psi_\omega] \tag{70}$$

View Source and

$$\gamma_{\omega r}=\frac{K_t}{J}\in[\Gamma_{m\omega},\Gamma_{M\omega}] \tag{71}$$

View Source

Denoting $\zeta_\omega=\left|\frac{K_t}{J}-\frac{\hat{K}_t}{\hat{J}}\right|=\left|\frac{1}{J}\left(\frac{3}{4}P\Phi_m\right)-\frac{1}{\hat{J}}\left(\frac{3}{4}P\hat{\Phi}_m\right)\right|$ satisfying the condition $\zeta_\omega\ll\frac{\hat{K}_t}{\hat{J}}$, we may choose the lower- and upper-bound $\Gamma_{m\omega},\Gamma_{M\omega}$ as follows

$$\begin{aligned}\Gamma_{m\omega}&=\frac{\hat{K}_t}{\hat{J}}-\zeta_\omega>0, &(72)\\ \Gamma_{M\omega}&=\frac{\hat{K}_t}{\hat{J}}+\zeta_\omega>0 &(73)\end{aligned}$$

View Source

The velocity control input is given as

$$i^*_q=i^*_{q,eq}+\tilde{i}^*_q \tag{74}$$

View Source and

$$\tilde{i}^*_q=i_{q1}+i_{q2}, \tag{75}$$

View Source where

$$\begin{aligned}\dot{i}_{q1}&=-W_{\omega r}\,\mathrm{sgn}(s_{\omega r}) &(76)\\ i_{q2}&=\begin{cases}-\lambda_{\omega r}|s_0|^p\,\mathrm{sgn}(s_{\omega r}) & |s_{\omega r}|>|s_0|\\ -\lambda_{\omega r}|s_{\omega r}|^p\,\mathrm{sgn}(s_{\omega r}) & |s_{\omega r}|\le|s_0|\end{cases} &(77)\end{aligned}$$

View Source

The sufficient conditions for finite-time convergence to the sliding surface are summarized as follows

$$\begin{aligned}W_{\omega r}&>\frac{\Psi_{\omega r}}{\Gamma_{m\omega}} &(78)\\ \lambda^2_{\omega r}&\ge\frac{4\Psi_{\omega r}}{\Gamma^2_{m\omega}}\frac{\Gamma_{M\omega}(W_{\omega r}+\Psi_{\omega r})}{\Gamma_{m\omega}(W_{\omega r}-\Psi_{\omega r})} &(79)\\ 0&<p\le 0.5 &(80)\end{aligned}$$

View Source

The controller can be simplified by selecting $s_0=\infty$. Hence, $\tilde{i}^*_q$ is obtained as

$$\tilde{i}^*_q=-\lambda_{\omega r}|s_{\omega r}|^{1/2}\,\mathrm{sgn}(s_{\omega r})-W_{\omega r}\int\mathrm{sgn}(s_{\omega r})dt \tag{81}$$

View Source

SECTION VI.

Experimental Results

A. Computer Simulation Results

The proposed field oriented sliding mode control algorithms have been examined with computer simulation studies. The testing SPM parameters are specified in Table I. The wheel-connected SPM serves as the traction motor of a heavy-duty vehicle, and we can control the torque of each wheel independently. For PI-based traditional field oriented control, the design parameters for all PI-controllers are Ki=5,Kp=50, which are fine-tuned to reduce the response overshoot and oscillation.

TABLE I Wheel-Connected SPM Specifications

Motor power	$80kW$
Armature winding resistance	$R_s = 6.5m\Omega$
d- and q-axis stator inductance	$L = 0.538mH$
Permanent magnet rotor flux linkage	$\Phi_m = 0.162Wb$
Number of stator poles	$P = 6$
Viscous friction coefficient	$B = 0.0001N.m.sec/rad$
Wheel inertia	$J = 8.2kg \cdot m^2$

Fig. 3 shows the rotor speed response. The load toque is changed from 0 Nm to 25 Nm at the time instant of 3 sec. The reference speed is increased from 500 rpm to 1000 rpm at the time instant of 5 sec. The higher-order sliding mode controller shows shorter rise-time, and less chattering compared with the first-order scheme. And the traditional PI-based field oriented control shows the slowest response time, highest sensitivity to external load change, and unsatisfactory speed regulation performance with significant overshoots and undershoots.

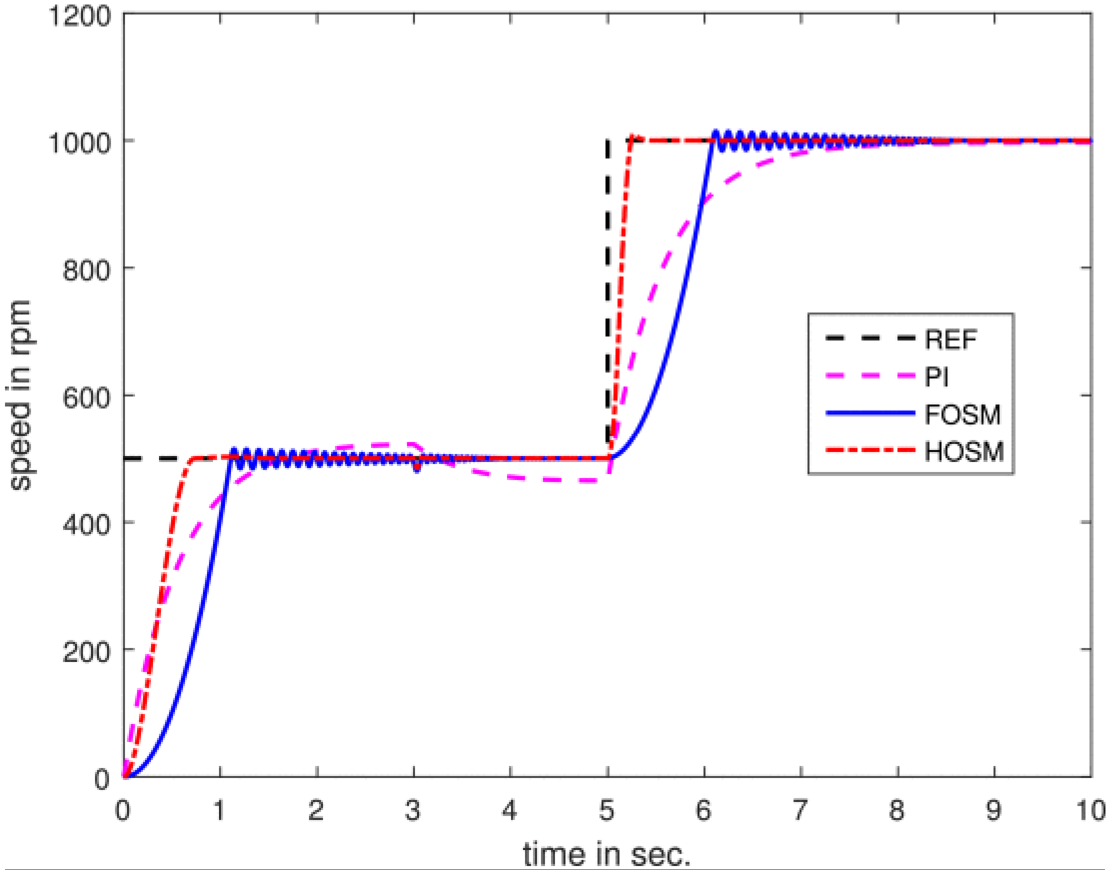

Fig. 3.

Speed response to reference speed and load torque changes.

View All

Fig. 4 shows the zoomed-in view of Fig. 3 speed response from 2.95 sec. to 3.15 sec. The sudden load change at 3 sec. in shown in greater detail. The higher-order sliding mode controller provides a faster response to the external load toque change from 0 to 25 Nm. The response of first-order controller can be improved by increasing the gains of switching control at the cost of much excessive chattering phenomenon. PI-based field oriented control shows the slowest response to the external load change with inadequate speed regulations.

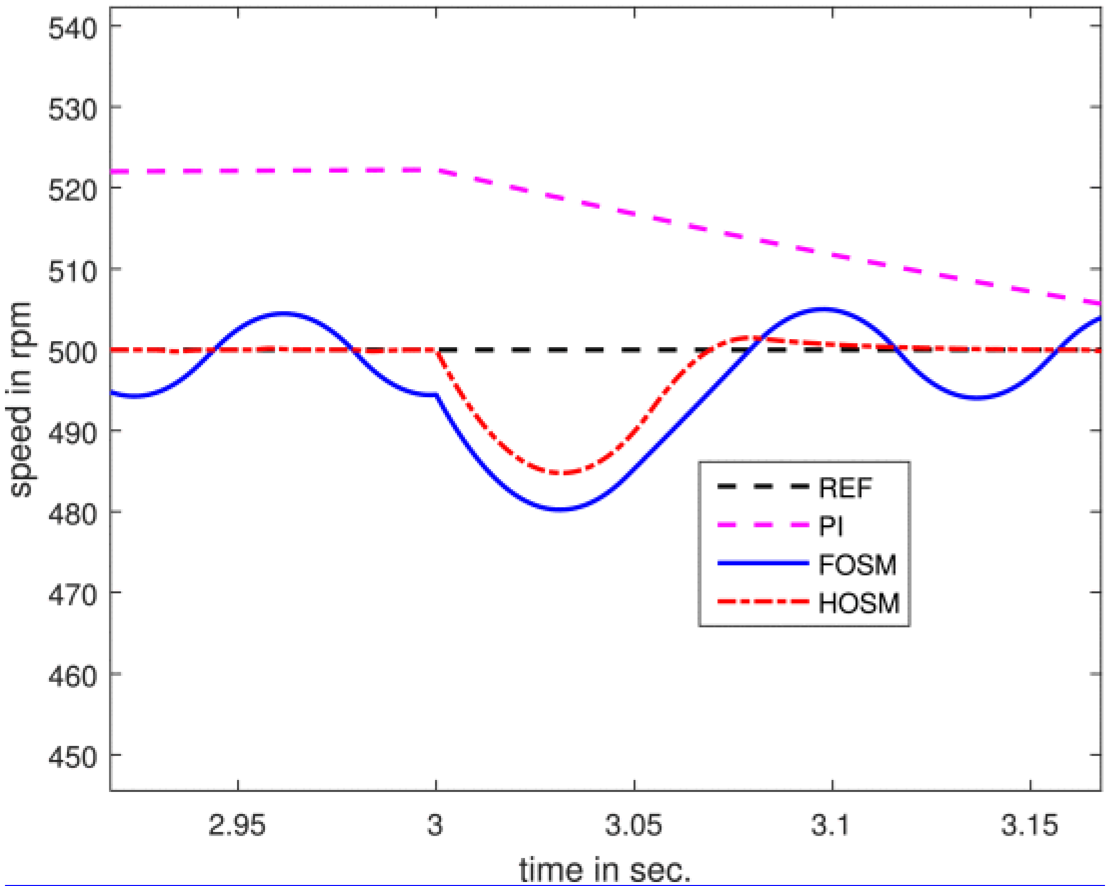

Fig. 4.

Speed response to load toque change at 3 sec.

View All

Stator current iq during the load toque and reference speed change is shown in Fig. 5. The switching control in the first-order scheme causes a high amplitude oscillation in the q -axis current in order to track the reference, and reject external disturbances and parameter uncertainties. The pronounced chattering is effectively reduced in the higher-order sliding mode controller. We did not include the traditional PI-based field oriented control iq response curve in Fig. 5, since the iq current with PI-control is significantly higher as shown in Fig. 6. Greater stator current iq means that the traditional PI-based field oriented control (PI-FOC) based motor drive consumes significantly more electrical power from the battery pack.

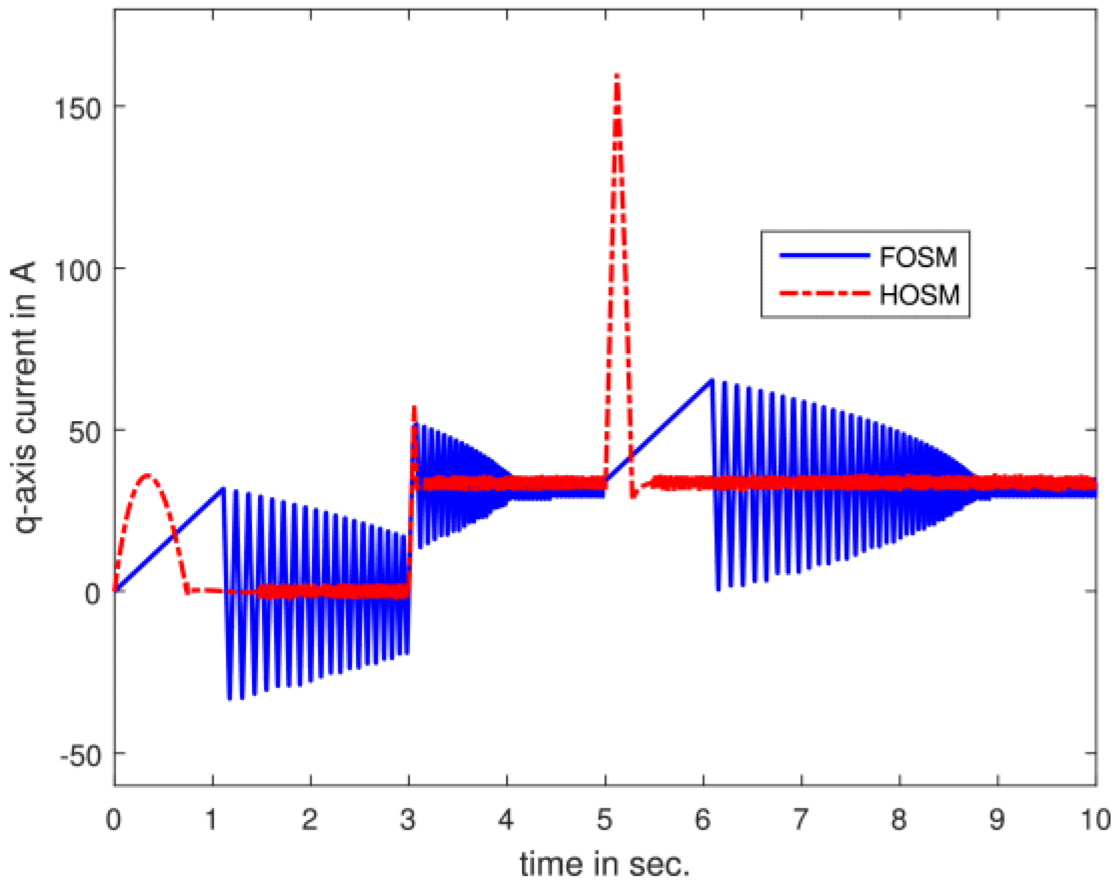

Fig. 5.

iq response to reference speed and load torque changes with the field oriented sliding mode control (FOSMC).

View All

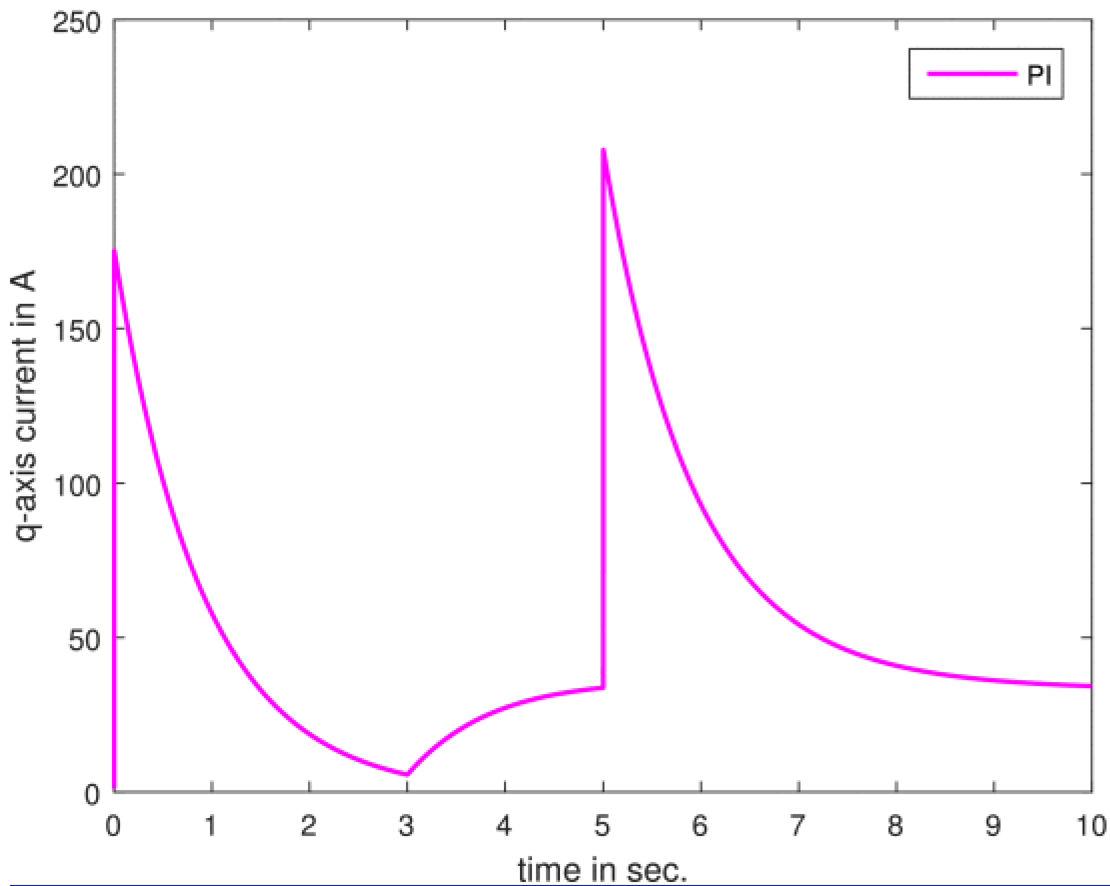

Fig. 6.

iq response to reference speed and load torque changes with the traditional PI-based field oriented control (PIFOC).

View All

Stator current id is regulated to zero by the first- and higher-order sliding mode scheme, for achieving the field-oriented control performance, as shown in Fig. 7. A closer look of the id response is shown in Fig. 8, which shows the significant chattering reduction by using the super-twisting algorithm (STA) based higher-order field oriented sliding mode control.

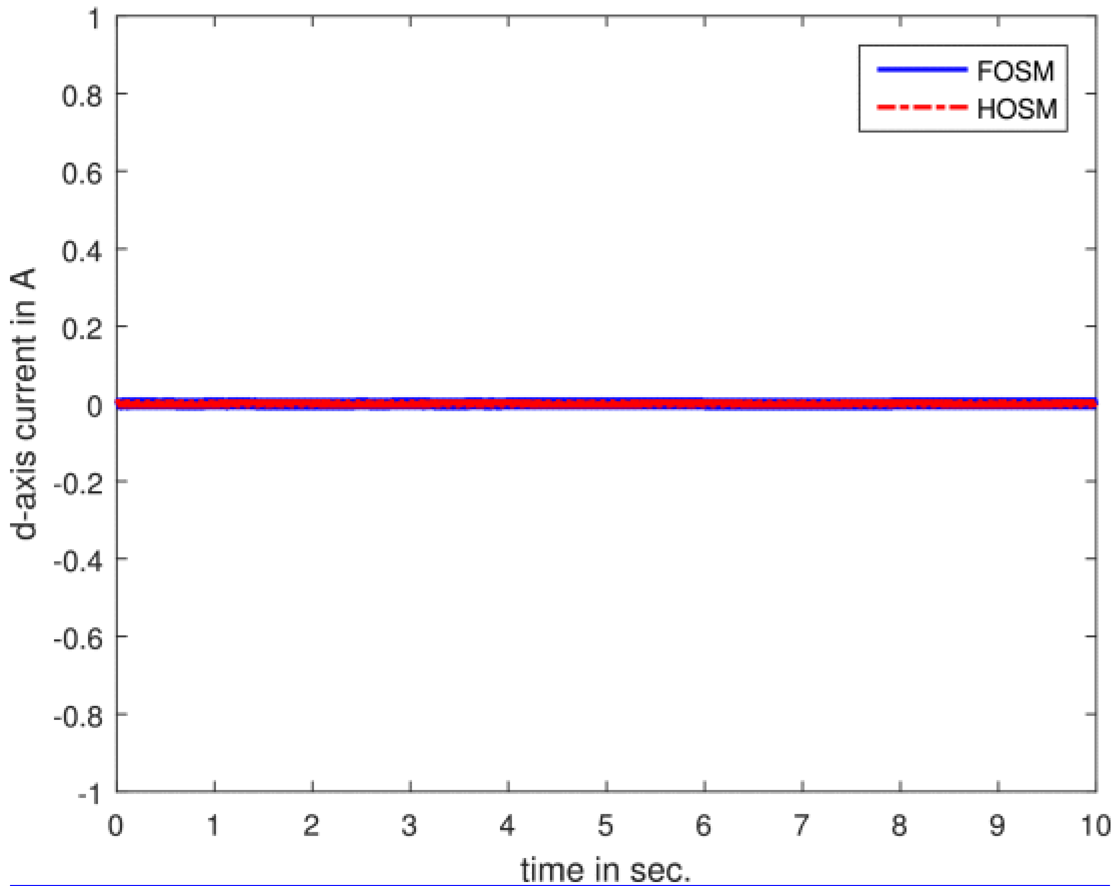

Fig. 7.

id response to reference speed and load torque changes with the field oriented sliding mode control (FOSMC).

View All

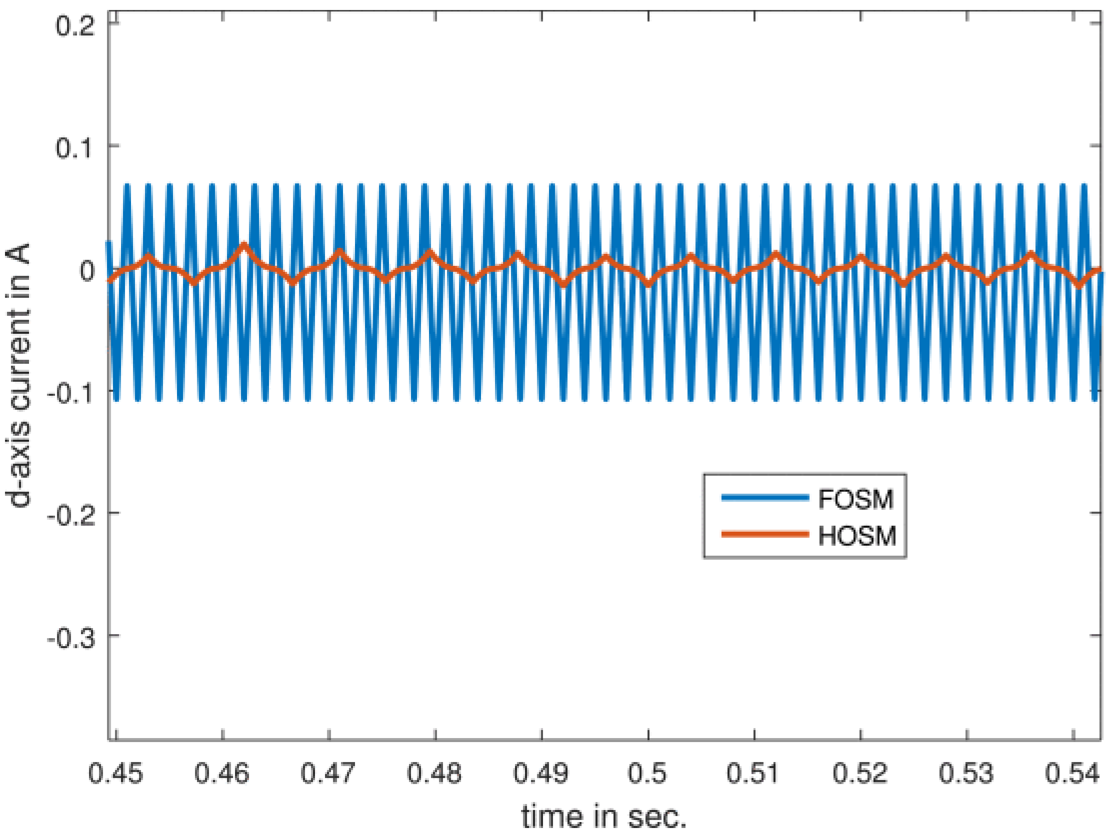

Fig. 8.

zoomed-in id response with the field oriented sliding mode control (FOSMC).

View All

Again, we did not include the traditional PI-based field oriented control id response curve in Fig. 7, since the id current with PI-control is significantly larger in magnitude as shown in Fig. 9. Greater stator current id means that the traditional PI-based field oriented controlled motor drives have greater electrical power usage from the battery pack. The proposed field oriented sliding mode control contributes significantly to the energy saving of battery-pack.

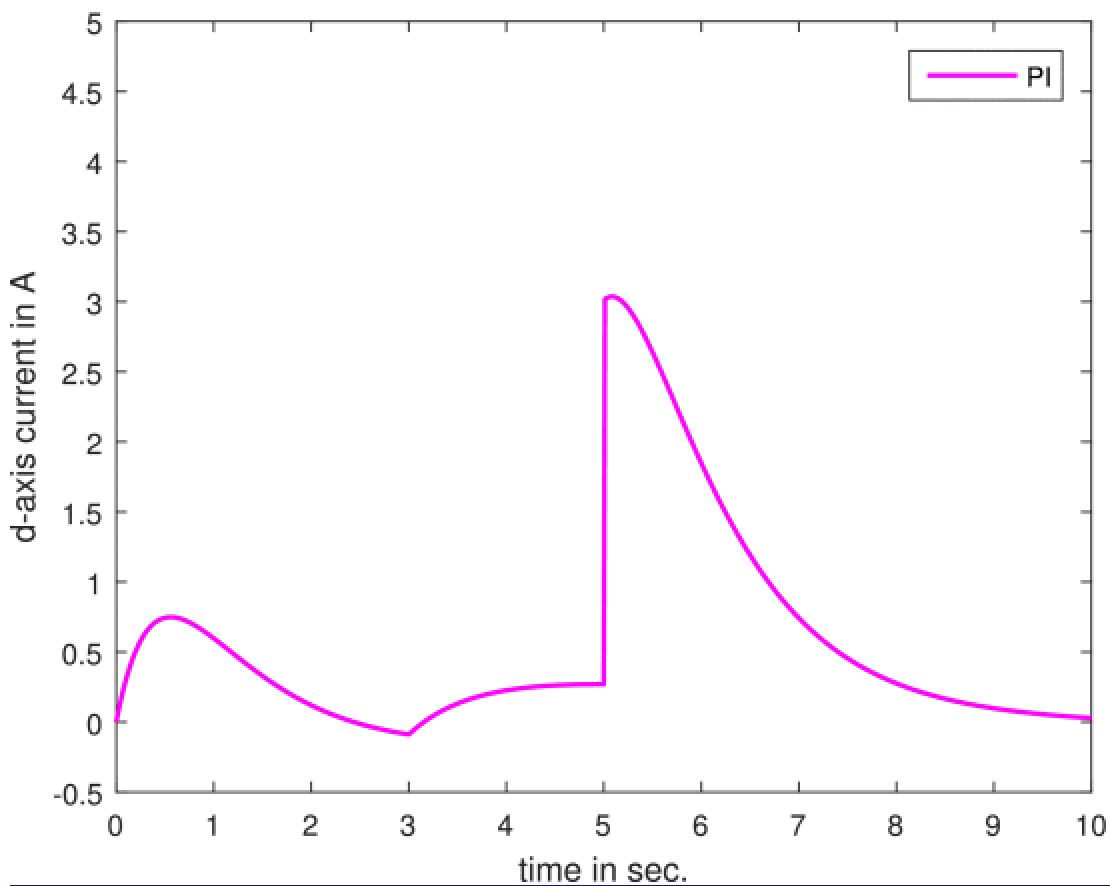

Fig. 9.

id response to reference speed and load torque changes with the traditional PI-based field oriented control (PIFOC).

View All

Based on the conducted simulation results, proportional-integral (PI) control is found to provide slower response in speed and torque control with pronounced overshoots and undershoots. PI-control is much more sensitive to external load changes, disturbances and modeling uncertainties. For different load values, the Kp,Ki control parameters should be readjusted, if possible, to provide a more decent torque and speed response. PI-control based motor drives consume greater amount of stator currents, which opens the new possibility that the battery usage can be further improved and optimized though advanced vehicle motion control technologies.

While both first- and higher-order field-oriented sliding mode controllers provide excellent dynamic performance in speed and torque response, computer simulation results verify that the higher-order sliding mode control method eliminates chattering in the first-order sliding mode scheme, becomes more robust to external load variations, rejects modeling parameters variation, and offers superior performance of quick and accurate torque generation for SPM motors.

B. Hardware Experimental Results

As shown in Fig. 10, the experiment is performed with a three-phase Anaheim Automation EMJ-04APA22, 0.4kW, 200V, 2.7A, 3000RPM permanent magnet synchronous motor. The SPM is powered by POWEREX PS21765, 600V, 20A, dual-in-line intelligent power module, which includes 6-IGBT inverter, and 3 half-bridge high-voltage integrated-circuit (HVIC) for IGBT gate driving. Space-vector pulse-width-modulation (SVPWM) is used as modulation strategy. The PWM voltage source inverter switching frequency is 10 kHz, while the PWMDAQ is 60kHz. The Texas Instruments 150MHz floating-point TMS320F28335 DSP controller is used, which is a 32 bit floating point digital signal processors with analog interface, RS232 and JTAG emulator port. The TMS320F28335 microprocessor is integrated on the TMDSCNCD28335 controlCARD board, which has analog-to-digital converter (A/D) with 16 channels. The proposed field oriented sliding mode control algorithms have been examined and implemented in real-time with the Texas Instrument TMS320F28335 DSP hardware platform. The parameters and specifications of Anaheim Automation EMJ-04APA22 PMSM are summarized in Table II.

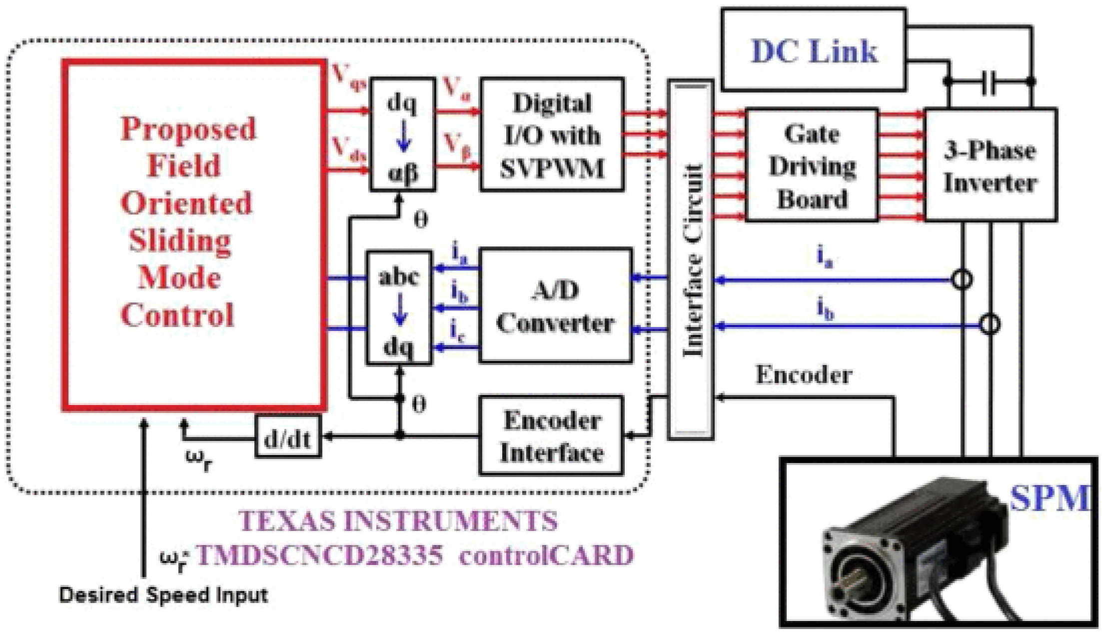

Fig. 10.

Experimental setup of prototype SPM drive system with Texas Instruments TMS320F28335 DSP.

View All

TABLE II Anaheim Automation EMJ-04APA22 SPM Parameters

Rated Power	$400W$
Rated Torque	$180oz.in$
Rated Voltage	$220Vrms$
Rated Current	$2.7A$
Rated Speed	$3000rpm$
Armature winding resistance	$R_s = 4.7\Omega$
d- and q-axis inductance	$L = 13.3mH$
Permanent magnet rotor flux linkage	$\Phi_m = 0.0785Wb$
Number of stator poles	$P = 8$
Viscous friction coefficient	$B = 0.0001N.m.sec./rad$
Rotor moment of inertia	$J = 0.00439oz.in.sec^2$
Weight	$5.52lbs$

Fig. 11 shows the experimental result of motor speed response with a reference speed of 2000 rpm. A step input speed reference is applied around 3 sec. Based on the DSP hardware experimental results, it is found that the higher-order field oriented sliding mode control (FOSMC) based SPM motor drive can provide quick and accurate real-time motion control. While PI-based traditional field oriented control shows overshoot and relatively slower response time. And the first-order field oriented sliding mode control shows quite significant chattering.

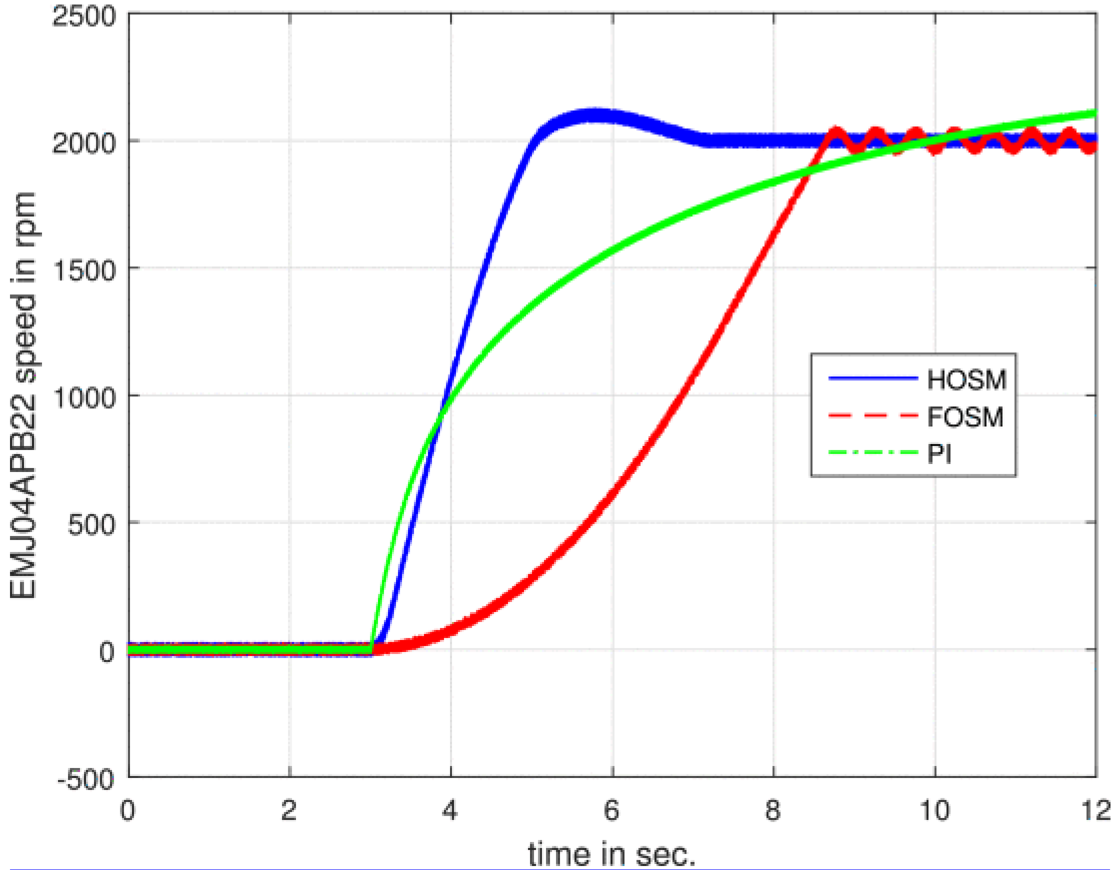

Fig. 11.

Anaheim Automation EMJ-04APA22 SPM speed response.

View All

SECTION VII.

Applications to Hybrid Electric Vehicles

Electrified vehicles is the most exciting target of advanced motion control technologies. The proposed field oriented sliding mode control (FOSMC) is applied for motion control of a heavy-duty diesel hybrid electric vehicle (HEV) to prove the effectiveness of this new method.

A. Vehicle Specifications

To reduce the energy consumption and improve vehicle's dynamic performance, the drive-train of this vehicle is composed of a V8 turbocharged diesel internal combustion engine (ICE) and 4 surface-mounted permanent magnet synchronous motors (SPMs). Regenerative braking is also considered in the computer simulation. Table III–VI summarize the detailed specifications of this heavy-duty diesel-HEV. And the overall vehicle structure is sketched in Fig. 12.

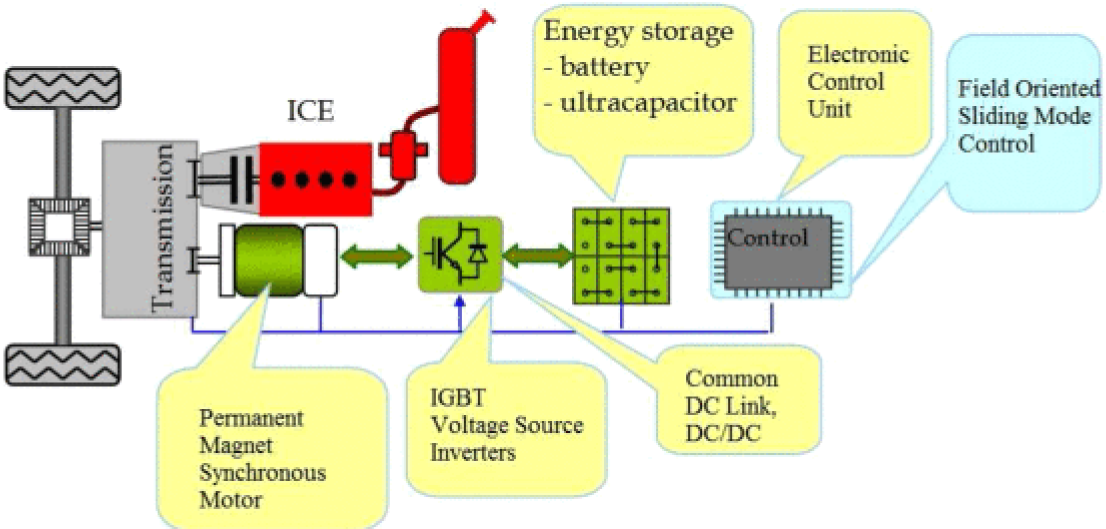

Fig. 12.

Hybrid electric vehicle block diagram.

View All

TABLE III Vehicle Specifications

Vehicle Mass	$10340kg$
Radius of Vehicle Wheel	$0.4131m$

TABLE IV Transmissions Specifications

Transmission: 1st Gear Ratio	3.45
Transmission: 2nd Gear Ratio	2.24
Transmission: 3rd Gear Ratio	1.41
Transmission: 4th Gear Ratio	1
Transmission: 1st Gear Efficiency	0.9893
Transmission: 2nd Gear Efficiency	0.966
Transmission: 3rd Gear Efficiency	0.9957
Transmission: 4th Gear Efficiency	1
Prop-shafts/Differential: Differential Drive Ratio	3.21
Prop-shafts/Differential: Differential Efficiency	0.96

TABLE V Diesel ICE Specifications

Configuration	V8 Turbocharged, Intercooled
Displacement	$7.3L$
Bore	$10.44cm$
Connecting Rod Length	$18.11cm$
Compression Ratio	$17.4cm$
Cutoff	2
Combustion Efficiency	1
Rated Peak Power	$210hp@2410rpm$,
Rated Peak Torque	$520lb\text{-}ft@1500rpm$,
Heating Value of Diesel QLHV	$43000000J/kg$
Fuel Density	800

TABLE VI Electric Motor Specifications

Electric Drivetrain	Wheel-Connected SPMs in Tab. I

The EPA Urban Dynamometer Driving Schedule (UDDS), which is commonly known as the ”LA4” or ”the city test” and represents city driving conditions [36], is applied as the driving schedule for this diesel-HEV simulation study.

B. Diesel-HEV Modeling and Vehicle Operation Modes

The power required by the diesel hybrid electric vehicle is

$$\dot{W}_{req}=[RL+(M+M_r)a]v, \quad (82)$$

View Source where $\dot{W}_{req}$ is the power required at the wheels to accelerate the vehicle and overcome drag, rolling resistance, and climbing force. The vehicle speed is v and the acceleration is a. The road load is

$$RL=\frac{1}{2}\rho v^2 C_D A+fW+W\sin\theta, \quad (83)$$

View Source where the first part is aerodynamic drag, the second part is the rolling resistance force and the third part is the climbing force. M is the vehicle full loading mass and the effective mass. The equivalent mass of the rotating components M_r can be obtained from the following equation:

$$M_r=M(1+0.04N_tN_f+0.0025N_t^2N_f^2)-M \quad (84)$$

View Source N_t and N_f are the gear ratios for the final drive (differential) and transmission.

The following notations are introduced before we discuss the vehicle operation modes: SOC denotes the state of charge (SOC) in the battery-pack; $\dot{W}_{req}$ is the required road-load power; $\dot{W}_{fric}$ is the power dissipated by friction brakes; η_f is the differential efficiency; η_t is the transmission efficiency; η_m is the motor drive efficiency; $\dot{W}_{engine}$ is the engine's output power; and $\dot{W}_{motor}$ is the SPM motor's output power.

Based on the power distribution between SPM motors and ICE, the following diesel-HEV operation modes are defined and applied for computer simulation studies. The power management logic governs different vehicle operation modes to achieve the power boosting during acceleration, and regenerative braking during deceleration.

- Pure electric vehicle (PEV) mode: When the required road-load power is positive $\dot{W}_{req}>0$, and the SOC is greater than a preset maximum threshold value SOC_{max}, i.e. $SOC>SOC_{max}$, the vehicle is completely driven by SPM motors and operated as a pure electric vehicle. Hence, when the battery is close to fully charged, the engine is shut off, the vehicle is operated as a PEV. The power required at the propeller shaft $\dot{W}_{req}\eta_f$ equals to the power delivered to the propeller shaft by traction motors.

$$\dot{W}_{req}\eta_f=\eta_m\dot{W}_{motor} \quad (85)$$

View Source

- Power boost mode: When the required road-load power $\dot{W}_{req}>0$, given battery state of charge is greater than a preset minimum threshold value SOC_{min}, but is less than a preset maximum threshold value, i.e., $SOC_{max}>SOC>SOC_{min}$, the following equation holds

$$\dot{W}_{req}\eta_f=\eta_t\dot{W}_{engine}+\eta_m\dot{W}_{motor} \quad (86)$$

View Source

The power required at the propeller shaft equals to the power delivered to the propeller shaft by the engine and SPMs, which is $\eta_t\dot{W}_{engine}+\eta_m\dot{W}_{motor}$.

- Pure ICE mode: When $\dot{W}_{req}\geq 0$ and the battery needs to be charged $SOC<SOC_{min}$, the HEV is operated in all ICE mode. Thus, we have

$$\dot{W}_{req}\eta_f=\eta_t\dot{W}_{engine} \quad (87)$$

View Source

- Regenerative braking mode: When the vehicle is decelerating or declining a hill, the vehicle kinetic energy can be stored by operating the motor in the generator mode for recharging the battery. Under this condition, engine is shut off, and $\dot{W}_{req}\leq 0$. The power delivered to propeller shaft by the differential $\dot{W}_{req}\eta_f$ satisfies ηfW˙req=W˙motorηm+W˙fric(88)

View Source

C. Heavy-Duty Diesel-HEV Simulation Results

The computer simulation results for heavy-duty diesel hybrid electric vehicle (HEV) are summarized in this section. To demonstrate the effectiveness of the proposed field oriented sliding mode control (FOSMC) in vehicle motion control applications. Fig. 13 shows the first-order and higher-order field oriented sliding mode control based diesel-HEV track the scheduled speed for the entire drive cycle. Fig. 14 show the zoomed-in view of HEV speed response comparisons. It is found that the higher-order FOSMC (labeled as “HOSM”, and shown in red dash-dot line) tracks the reference speed (labeled as “REF”, and shown in black dashed line) more closely than the first-order FOSMC approach (labeled as “FOSM”, and shown in blue solid line) throughout the entire drive cycle.

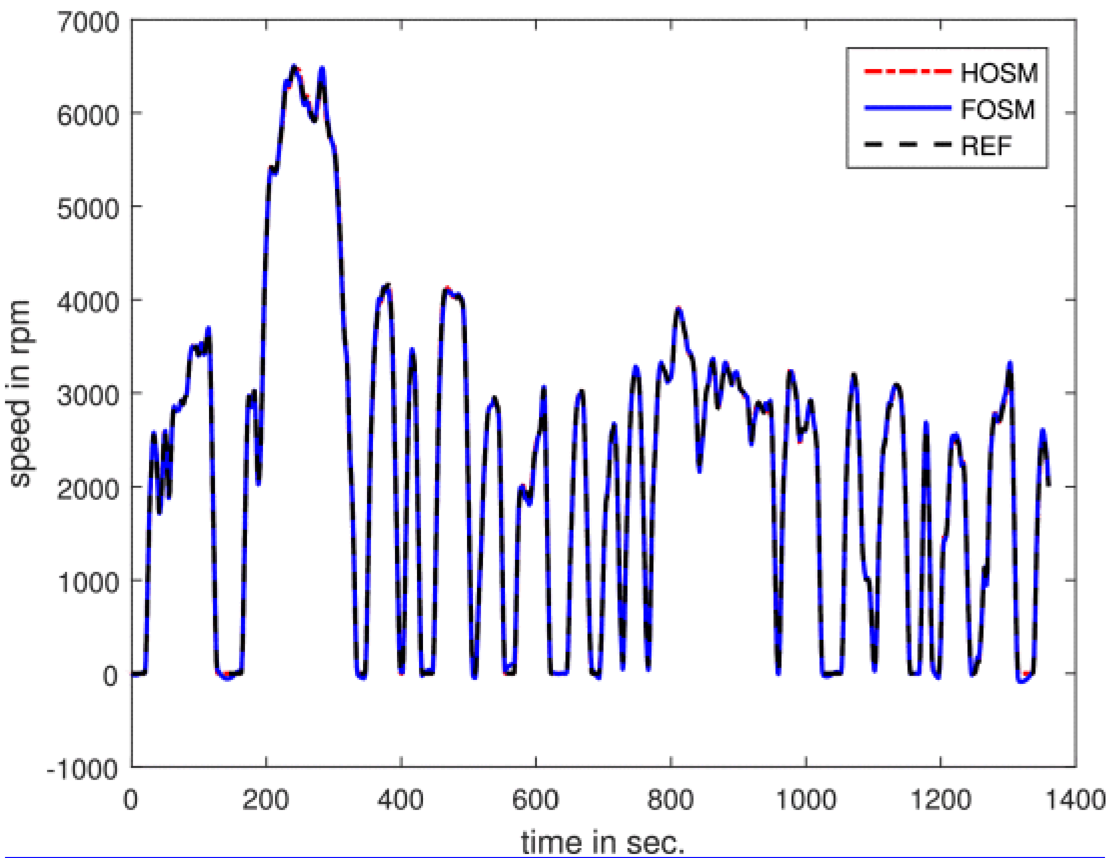

Fig. 13.

Diesel hybrid electric vehicle speed response in rpm.

View All

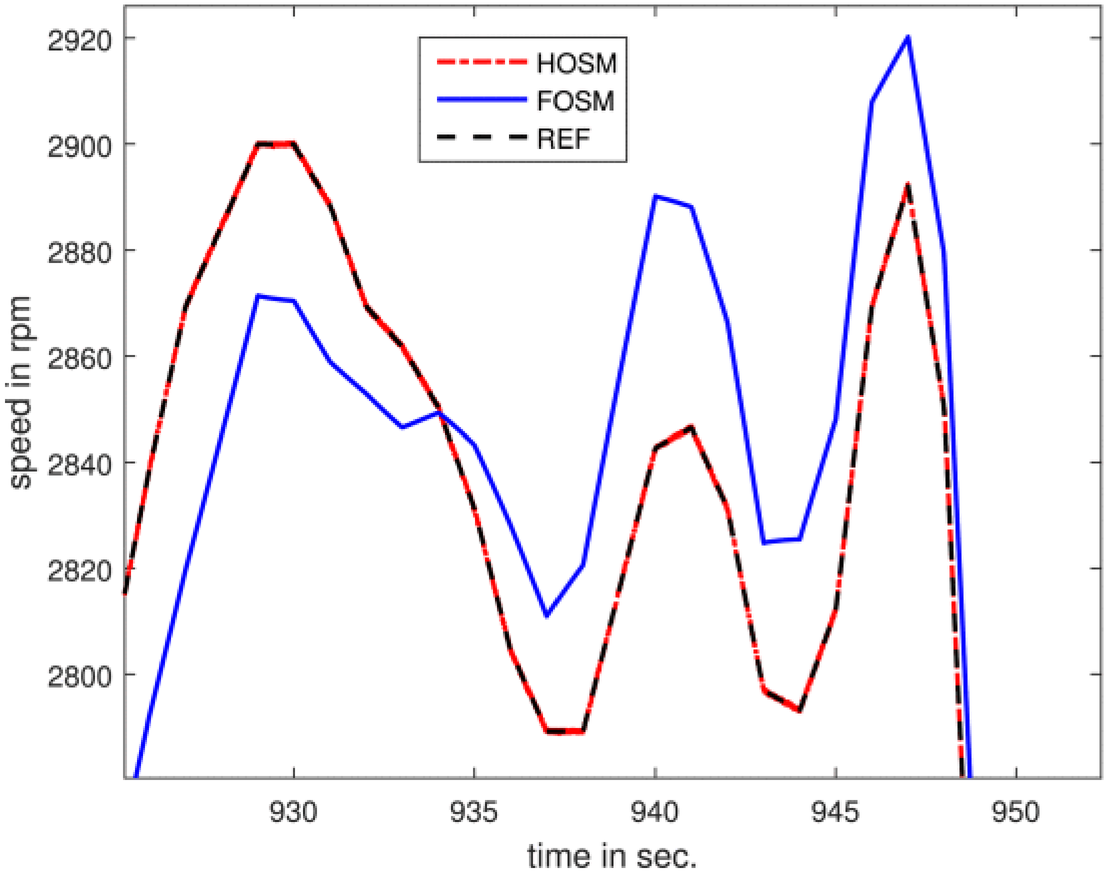

Fig. 14.

Zoomed-in view of the vehicle speed response in rpm.

View All

Fig. 15 shows the internal combustion engine's torque response. Fig. 16 shows the required vehicle power, the power from internal combustion engine, and the power from permanent magnet traction motors.

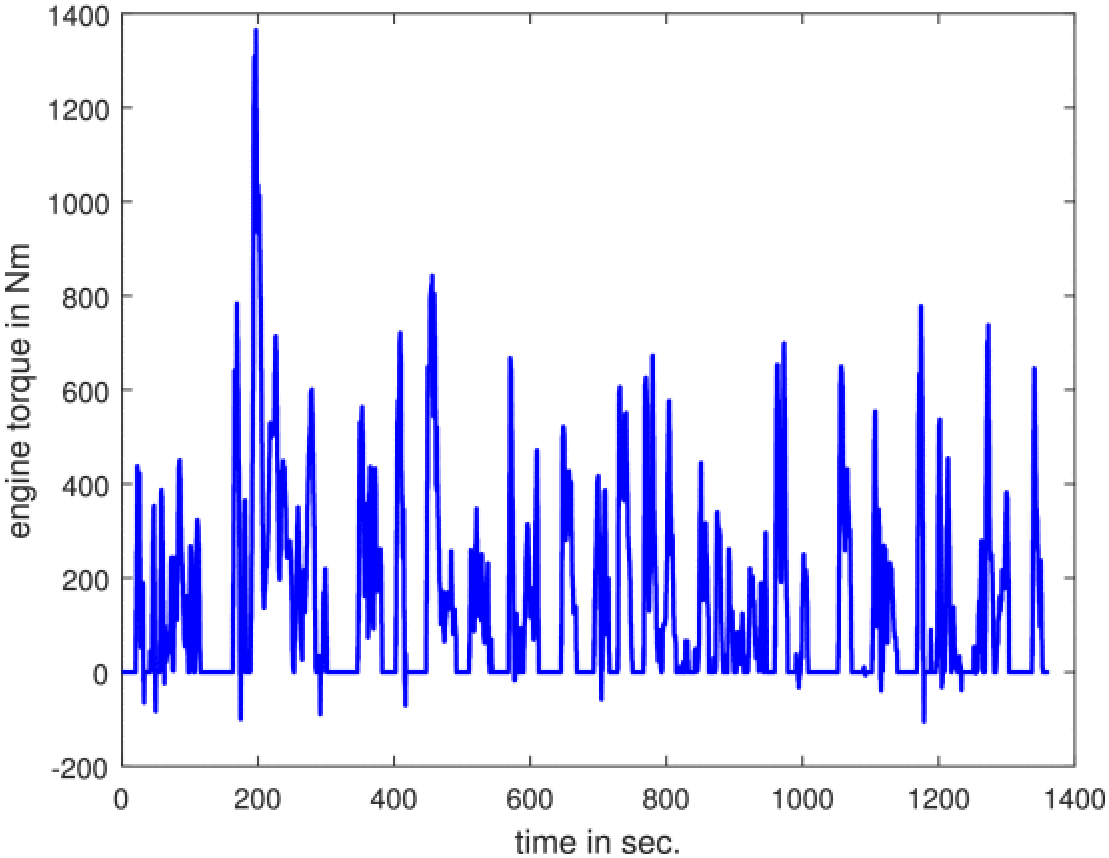

Fig. 15.

Internal combustion engine torque response.

View All

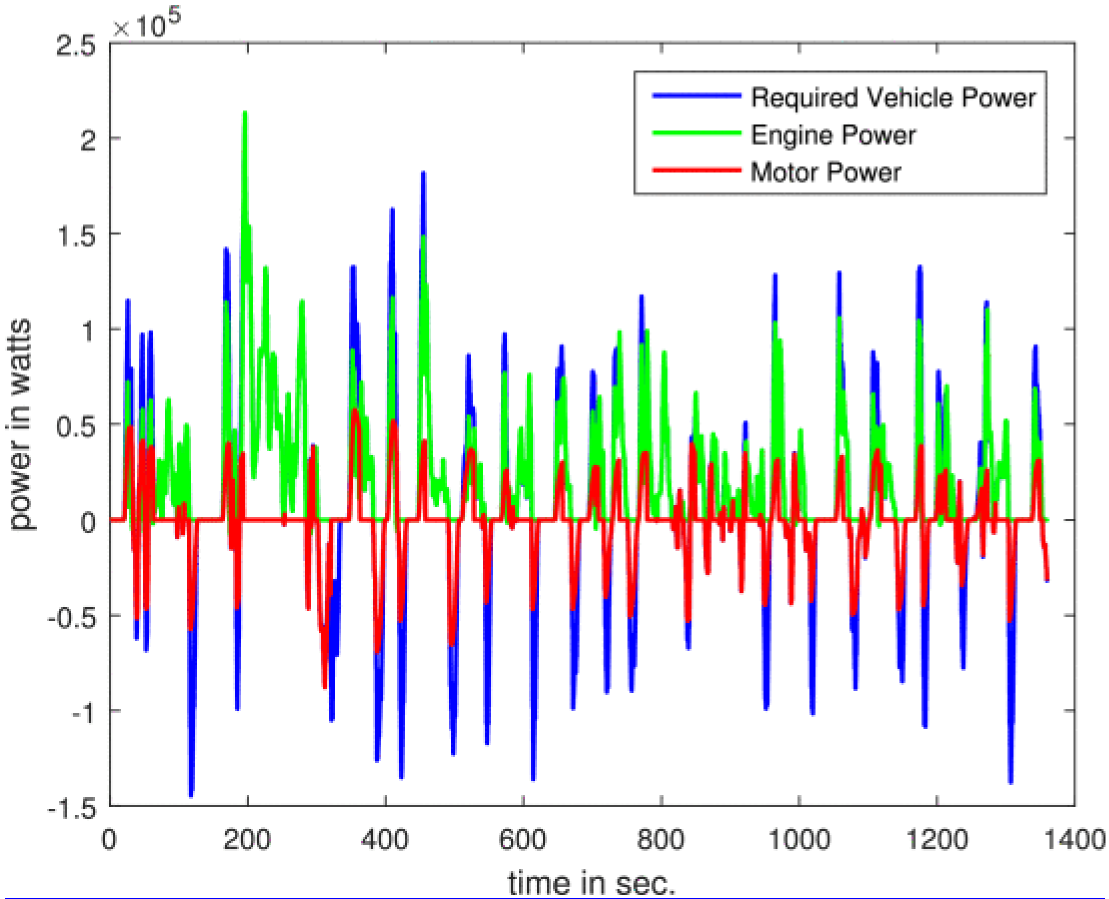

Fig. 16.

Vehicle required power, engine power and motor power.

View All

Fig. 17 and Fig. 18 compare the quadrature-axis stator current iq 's responses based on the first-order and higher-order field oriented sliding mode control approaches, respectively. Noted that the q-axis stator current iq is proportional to the developed motor torque for SPM motors. It can be found that chattering is much more pronounced in the first-order FOSMC's iq response.

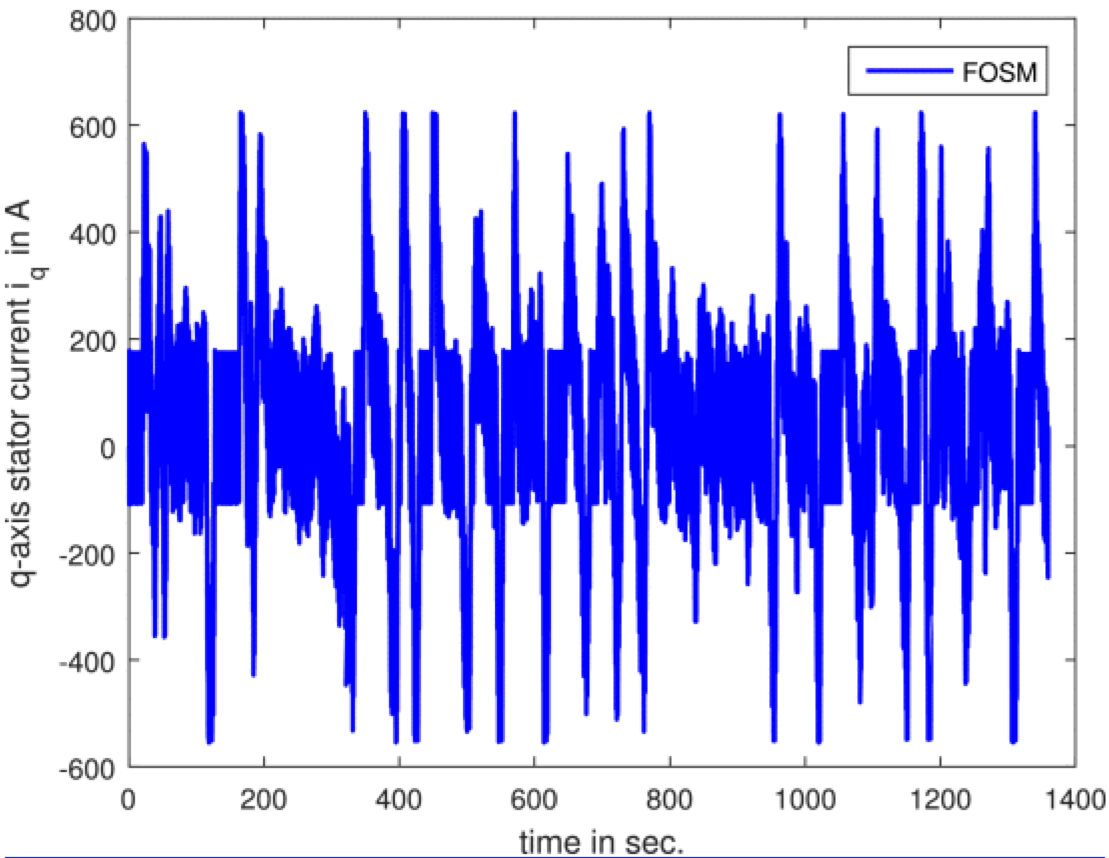

Fig. 17.

Quadrature-axis stator current using the first-order FOSMC.

View All

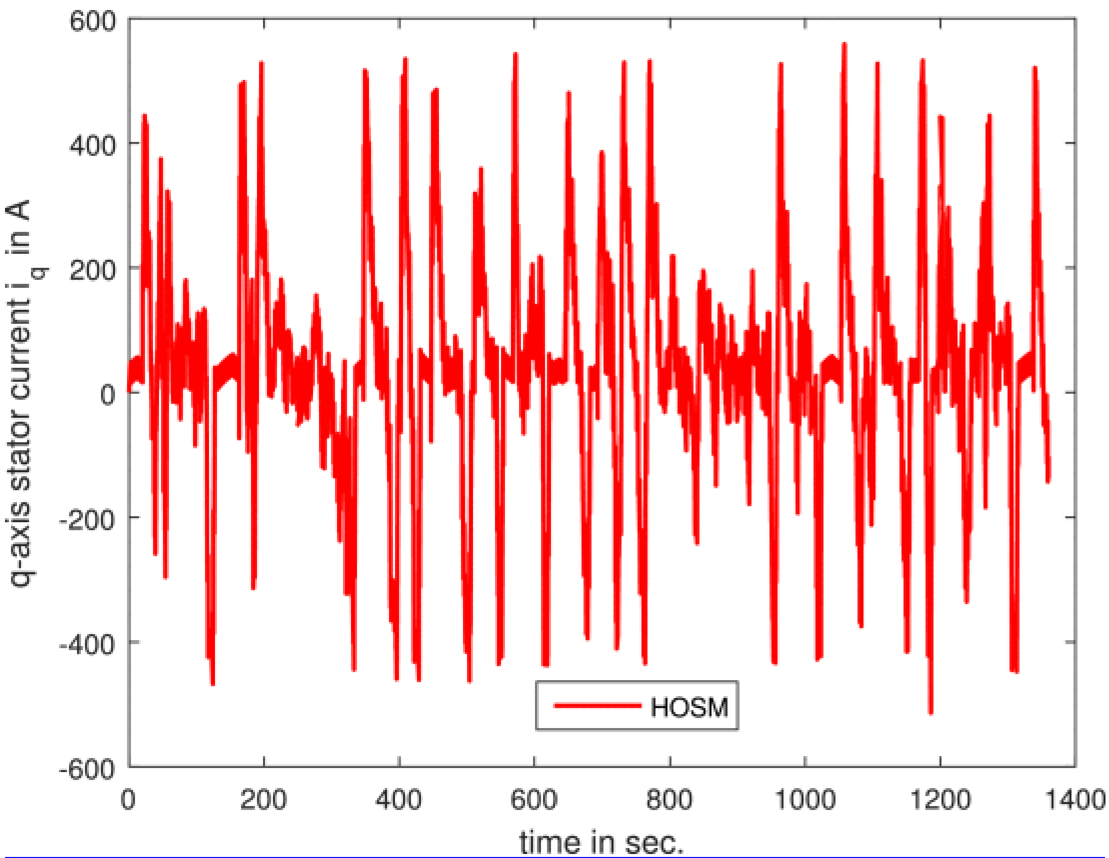

Fig. 18.

Quadrature-axis stator current using the higher-order FOSMC.

View All

Similarly, the direct-axis stator current id responses are summarized in Fig. 19 and Fig. 20. Fig. 19 is based on the first-order field oriented sliding mode control approach, and Fig. 20 is based on the higher-order approach. id is successfully regulated to be 0, in order to maximize the developed electromechanical torque of the PM traction motors. Again, chattering is much more noticeable in the first order FOSMC's id response.

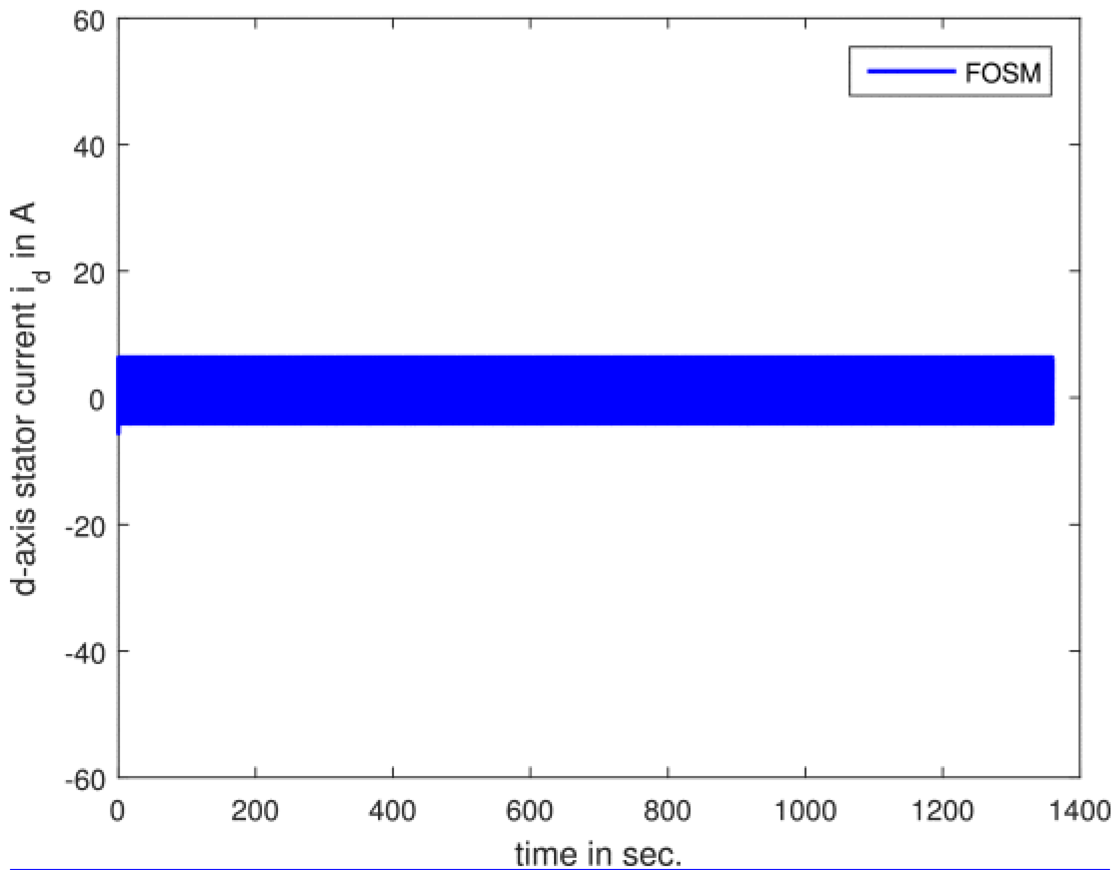

Fig. 19.

Direct-axis stator current using the first-order FOSMC.

View All

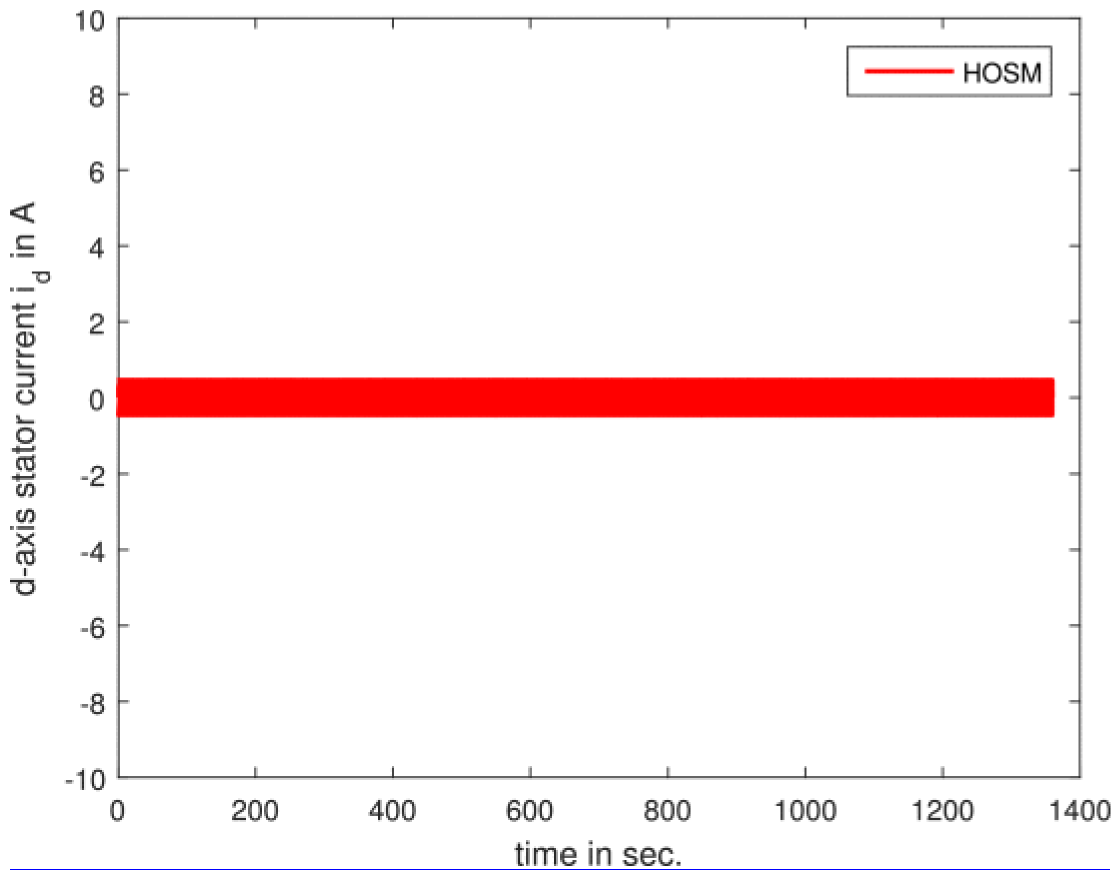

Fig. 20.

Direct-axis stator current using the higher-order FOSMC.

View All

Lastly, Fig. 21 and Fig. 22 compare the developed electromechanical torque response from each SPM traction motor by using the first-order and higher-order field oriented sliding mode control, respectively. The first-order field oriented sliding mode control shows conspicuous chattering, while the higher-order field-oriented sliding mode greatly reduces the chattering in torque response.

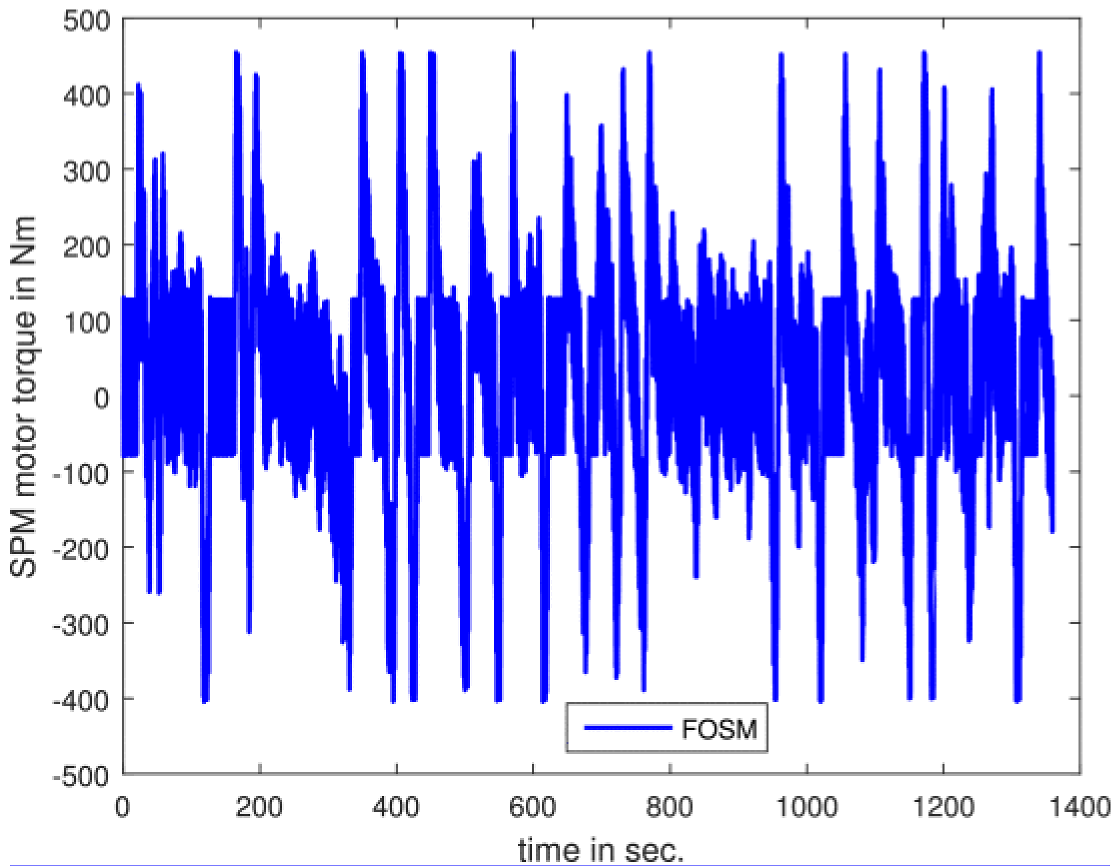

Fig. 21.

SPM traction motor torque response using the first-order FOSMC.

View All

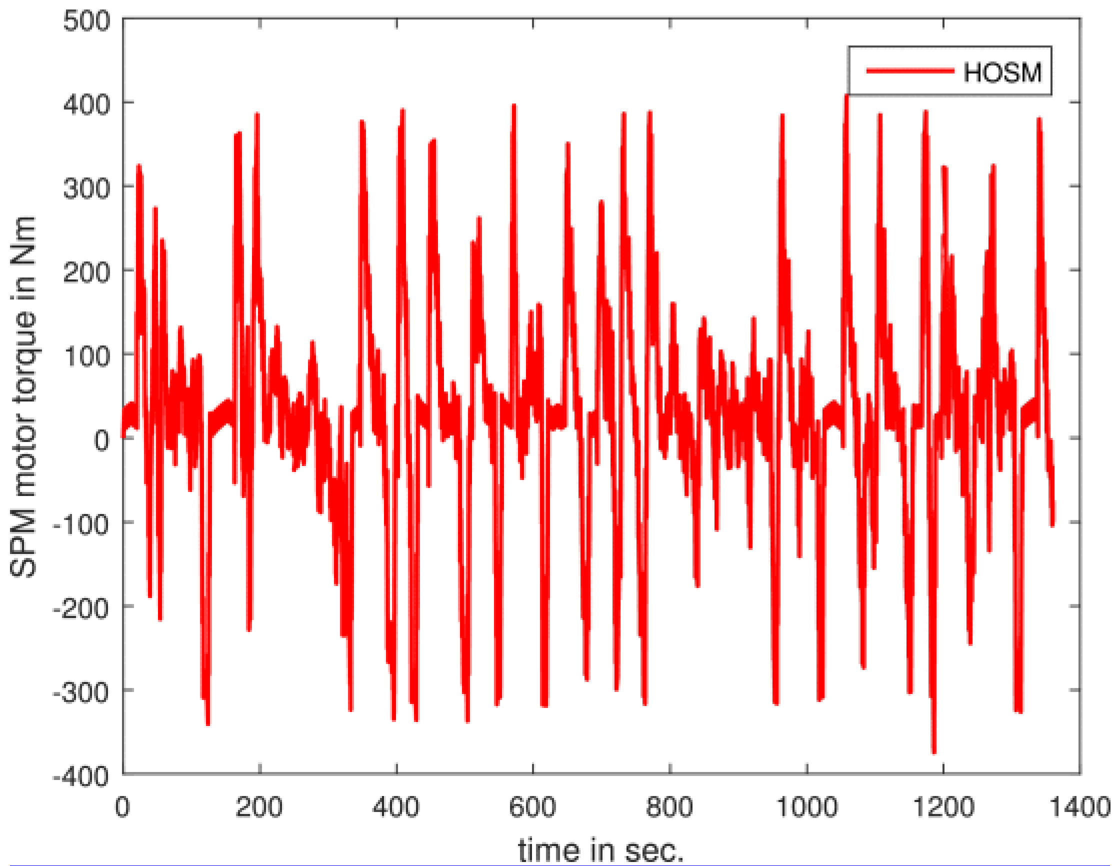

Fig. 22.

SPM traction motor torque response using the higher-order FOSMC.

View All

SECTION VIII.

Conclusion

This paper has proposed the novel theory, design, simulation and implementation of both first- and higher-order field oriented sliding mode control (FOSMC) of surface-mounted permanent magnet AC motors with applications to electrified vehicles. Hardware experimental results and computer simulation studies have demonstrated that the higher-order sliding mode controller is superior to the first-order scheme by offering a faster transient response and eliminating the chattering phenomenon. Furthermore, the proposed field oriented sliding mode control methods have also been successfully applied in permanent magnet traction motor control of a heavy-duty diesel hybrid electric vehicle tested under UDDS urban driving schedule.

References

1. Y. Hori, "Future vehicle driven by electricity and Control-research on four-wheel-motored ‘UOT electric march II", *IEEE Trans. Ind. Electron.*, vol. 51, no. 5, pp. 954-962, Oct. 2004.
2. I. Takahashi, T. Noguchi, "A new quick-response and high-efficiency control strategy of an induction motor", *IEEE Trans. Ind. Appl.*, vol. IA-22, no. 5, pp. 820-827, Sep. 1986.

3. L. Zhong, M. F. Rahman, W. Y. Hu, K. W. Lim, "Analysis of direct torque control in permanent magnet synchronous motor drives", *IEEE Trans. Power Electron.*, vol. 12, no. 3, pp. 528-536, May 1997.

4. G. S. Buja, M. P. Kazmierkowski, "Direct torque control of PWM inverter-fed AC motors—A survey", *IEEE Trans. Ind. Electron.*, vol. 51, no. 4, pp. 744-757, Aug. 2004.

5. Y. Zhang, J. Zhu, "Direct torque control of permanent magnet synchronous motor with reduced torque ripple and commutation frequency", *IEEE Trans. Power Electron.*, vol. 26, no. 1, pp. 235-248, Jan. 2011.

6. K. Gulez, A. Adam, H. Pastaci, "A novel direct torque control algorithm for IPMSM with minimum harmonics and torque ripples", *IEEE/ASME Trans. Mechatronics*, vol. 12, no. 2, pp. 223-227, Apr. 2007.

7. Y. Kung, M. Tsai, "FPGA-based speed control IC for PMSM drive with adaptive fuzzy control", *IEEE Trans. Power Electron.*, vol. 22, no. 6, pp. 2476-2486, Nov. 2007.

8. S. A. Zulkifli, M. Z. Ahmad, *Proc. Int. Conf. Electron. Devices Syst. Appl.*, pp. 290-293, 2011.

9. T. D. Do, S. Kwak, H. H. Choi, J. W. Jung, "Suboptimal control scheme design for interior permanent-magnet synchronous motors: An SDRE-based approach", *IEEE Trans. Power Electron.*, vol. 29, no. 6, pp. 3020-3031, Jun. 2014.

10. P. Medagam, T. Yucelen, F. Pourboghrat, "Adaptive SDRE-based nonlinear sensorless speed control for PMSM drives", *Proc. 39th North Amer. Power Symp.*, pp. 518-522, Sep. 2007.

11. A. Imura, T. Takahashi, M. Fujitsuna, T. Zanma, M. Ishida, "Instantaneous-current control of PMSM using MPC: Frequency analysis based on sinusoidal correlation", *Proc. IECON - 37th Annu. Conf. IEEE Ind. Electron. Soc.*, pp. 3551-3556, 2011.

12. B. Mobarakeh, F. Meibody-Tabar, F. Sargos, "A self organizing intelligent controller for speed and torque control of a PMSM", *Proc. IEEE Ind. Appl. Conf.*, pp. 1283-1290, 2000.

13. F. F. M. El-Sousy, "Intelligent optimal recurrent wavelet Elman neural network control system for permanent-magnet synchronous motor servo drive", *IEEE Trans. Ind. Inform.*, vol. 9, no. 4, pp. 1986-2003, Nov. 2013.

14. M. A. M. Cheema, J. E. Fletcher, D. Xiao, M. F. Rahman, "A linear quadratic regulator-based optimal direct thrust force control of linear permanent-magnet synchronous motor", *IEEE Trans. Ind. Electron.*, vol. 63, no. 5, pp. 2722-2733, May 2016.

15. S. M. Sue, C. T. Pan, "Voltage-constraint-tracking-based field weakening control of IPM synchronous motor drives", *IEEE Trans. Ind. Electron.*, vol. 55, no. 1, pp. 340-347, Jan. 2008.

16. H.-H. Chiang, K.-C. Hsu, I.-H. Li, "Optimized adaptive motion control through an SoPC implementation for linear induction motor drives", *IEEE/ASME Trans. Mechatronics*, vol. 20, no. 1, pp. 348-360, Feb. 2015.

17. M. Bodson, J. Chiasson, R. Novotnak, R. Rekowski, "High performance nonlinear feedback control of a permanent magnet stepper motor", *IEEE Trans. Control Syst. Technol.*, vol. 1, no. 1, pp. 5-14, Mar. 1993.

18. F. Aghili, "Optimal feedback linearization control of interior PM synchronous motors subject to time-varying operation conditions minimizing power loss", *IEEE Trans. Ind. Electron.*, vol. 65, no. 7, pp. 5414-5421, Jul. 2018.

19. S. Morimoto, M. Sanada, Y. Takeda, "Wide-speed operation of interior permanent magnet synchronous motors with high-performance current regulator", *IEEE Trans. Ind. Appl.*, vol. 30, no. 4, pp. 920-926, Jul. 1994.

20. H. Nakai, H. Ohtani, E. Satoh, Y. Inaguma, "Development and testing of the torque control for the permanent-magnet synchronous motor", *Proc. 27th Annu. Conf. IEEE Ind. Electron. Soc.*, vol. 2, pp. 1463-1468, 2001.

21. S. Morimoto, K. Hatanaka, Y. Tong, Y. Takeda, T. Hirasa, "High performance servo drive system of salient pole permanent magnet synchronous motor", *Proc. Conf. Rec. 1991 IEEE Ind. Appl. Soc. Annu. Meet.*, vol. 1, pp. 463-468, Sep. 1991.

22. G. Rang, J. Lim, K. Nam, H.-B. Ihm, H.-G. Kim, "A MTPA control scheme for an IPM synchronous motor considering magnet flux variation caused by temperature", *Proc. IEEE 19th Annu. Appl. Power Electron. Conf. Expo.*, vol. 3, pp. 1617-1621, 2004.

23. B. Cheng, T. R. Tesch, "Torque feedforward control technique for permanent-magnet synchronous motors", *IEEE Trans. Ind. Electron.*, vol. 57, no. 3, pp. 969-974, Mar. 2010.

24. X. Zhang, L. Sun, K. Zhao, L. Sun, "Nonlinear speed control for PMSM system using sliding-mode control and disturbance compensation techniques", *IEEE Trans. Power Electron.*, vol. 28, no. 3, pp. 1358-1365, Mar. 2013.

25. S. Di Gennaro, J. Rivera Domínguez, M. A. Meza, "Sensorless high order sliding mode control of induction motors with core loss", *IEEE Trans. Ind. Electron.*, vol. 61, no. 6, pp. 2678-2689, Jun. 2014.

26. Z. Qiao, T. Shi, Y. Wang, Y. Yan, C. Xia, X. He, "New sliding-mode observer for position sensorless control of permanent-magnet synchronous motor", *IEEE Trans. Ind. Electron.*, vol. 60, no. 2, pp. 710-719, Feb. 2013.

27. M. Reichhartinger, M. Horn, "Sliding-mode control of a permanent magnet synchronous motor with uncertainty estimation", *Int. J. Elect. Comput. Eng.*, vol. 4, no. 11, pp. 1637-1640, 2010.

28. S. Li, M. Zhou, X. Yu, "Design and implementation of terminal sliding mode control method for PMSM speed regulation system", *IEEE Trans. Ind. Inform.*, vol. 9, no. 4, pp. 1879-1891, Nov. 2013.

29. D. Biel, F. Guinjoan, E. Fossas, J. Chavarria, "Sliding-mode control design of a boost-buck switching converter for AC signal generation", *IEEE Trans. Circuits Syst. I Reg. Papers*, vol. 51, no. 8, pp. 1539-1551, Aug. 2004.

30. A. Levant, L. Fridman, "Higher-order sliding modes", *Proc. Sliding Mode Control Eng.*, pp. 53-101, 2002.

31. K. Young, V. Utkin, U. Ozguner, "A control engineer's guide to sliding mode control", *Proc. IEEE Int. Workshop Variable Struct. Syst.*, pp. 1-14, Dec. 1996.

32. W. Perruquetti, J. P. Barbot, Sliding Mode Control in Engineering., Boca Raton, FL, USA:CRC Press, 2002.

33. M. Reitz, X. Wang, P. Gu, "Robust sliding mode control of permanent magnet synchronous motor drives", *Proc. IEEE Transp. Electrific. Conf. Expo*, pp. 1-6, 2016.

34. J. Hostettler, X. Wang, "Sliding mode control of a permanent magnet synchronous generator for variable speed wind energy conversion systems", *Proc. Amer. Control Conf.*, pp. 4982-4987, Jul. 2015.

35. T. M. Jahns, G. B. Kliman, T. W. Neumann, "Interior permanent magnet synchronous motors for adjustable-speed drives", *IEEE Trans. Ind. Appl.*, vol. IA-22, no. 4, pp. 738-747, Jul. 1986.

36. "EPA Urban Dynamometer Driving Schedule (UDDS) Emission Standards Reference Guide US EPA", Mar. 2016, [online] Available: www.epa.gov.